Homopolymer Adsorption and Pattern Recognition on Hexagonal Surfaces: A Replica-Exchange Monte Carlo Study

by

Benjamin Liewehr

(Under the Direction of Michael Bachmann)

Abstract

The recognition of a hexagonal substrate pattern by a coarse-grained flexible homopolymer during the surface adsorption process is investigated using parallel tempering (replica-exchange) Monte Carlo simulations. The strength of the interaction between a grafted homopolymer chain and a honeycomb surface, which is based on a standard Lennard-Jones potential, is changed systematically to study different hexagonally patterned substrate materials and miscellaneous implicit solvents. Introducing specific order parameters, 16 structural phases are identified at different surface adsorption strengths and temperatures and are classified into expanded, globular, droplet, semi-spherical and compact phases. Properties of structural phase transitions and representative polymer conformations are discussed to construct a complete structural hyperphase diagram for a polymer with 55 monomers. Finally, a detailed analysis of structural properties in the regime of solid-like conformations leads to the identification of different pattern recognition strategies due to conflicting ordering effects, induced by intramolecular and monomer-substrate interactions.

Index words: Pattern recognition, polymer adsorption, polymer grafting, structural phase transition, hyperphase diagram, hexagonal surface, honeycomb lattice, graphene, surface enhancement, polymer coatings

Homopolymer Adsorption and Pattern Recognition on Hexagonal Surfaces: A Replica-Exchange Monte Carlo Study

by

Benjamin Liewehr

B.A., Universität Rostock, Germany, 2014

A Thesis Submitted to the Graduate Faculty
of The University of Georgia in Partial Fulfillment
of the
Requirements for the Degree

Master of Science

Athens, Georgia

2016

Homopolymer Adsorption and Pattern Recognition on Hexagonal Surfaces: A Replica-Exchange Monte Carlo Study

by

Benjamin Liewehr

Approved:

Major Professor: Michael Bachmann

Committee: David P. Landau
Steven P. Lewis

Electronic Version Approved:

Suzanne Barbour
Dean of the Graduate School
The University of Georgia
May 2016

Homopolymer Adsorption and Pattern Recognition on Hexagonal Surfaces: A Replica-Exchange Monte Carlo Study

Benjamin Liewehr

April 7, 2016

Acknowledgments

First, I would like to acknowledge Dr. Bachmann's scientific support and his service as my academic advisor during the past four semesters. After I arrived in 2014 with a bachelors degree from the Universität Rostock, Germany at the University of Georgia, he initiated enthusiastically a research project which lead to very interesting results, presented in this thesis. Moreover, due to the fruitful work on this project, we were able to present first results at the Universidade Federal de Mato Grosso, Cuiabá, Brazil and on the VIIIth Brazilian Meeting on Simulational Physics, Florianopolis. I am much obliged that Dr. Bachmann supported me with these opportunities.

During my stay at the Department of Physics and Astronomy, I learned in many courses physics but also gained an understanding of the work environment of academic research enterprises. In this regard I am especially grateful for the many lessons I could learn from the Director of the Center for Simulational Physics Dr. Landau, who provides his students during his classes on Monte Carlo techniques and Molecular Dynamics methods often with insights behind the scenes of the scientific world. Mentioning the interesting "Monte Carlo trajectories" of scientific results and also of researchers or former students who created these findings, lead to a vital understanding of different path ways that other scientists took. Since Dr. Landau offers students to engage also outside of the classroom, for example during the lunch breaks in discussions, I was also able to experience how strategic decisions about different aspects of university and research are approached. I know Dr. Landau as an

approachable and considerate director, who is concerned about the well being of all members of the center. Balancing professional guidance with human understanding, Dr. Landau exemplifies leadership to the students and members of the center.

For a similar aspect of the graduate education I would like to thank Dr. Lee, an outstanding teacher who understands to emphasize the miracles behind physical effects, the beauty of theory, but most importantly, the appreciation of the achievements of others, achievements of world famous physicists and also the results of students. During his classes on chaos, Hamilton-Jacobi theory and statistical mechanics he explained under which circumstances far reaching results were obtained and exemplified a deeply grateful attitude.

One important character in the physics department I like to thank for his advise about how to understand career, people and life is Dr. Magnani. From the first day on, where he helped me to arrange the course work schedule, I got to know him as a very honest and straight-out professor, who has an open ear for graduate students. I would like to thank Dr. Magnani for providing well grounded reflections and sharing his unbiased opinion regardless of the possible outcome.

In the class on group theory Dr. Lewis exemplified excellence in teaching. I would like to thank him for creating exciting lectures by encouraging open discussions in class, coupled with concise, yet accurate derivations on the board. Dr. Lewis is also outside of class an easily approachable professor, who can offer helpful advise. In this context I appreciate his refreshing, very American sense of humor which especially students from the old world will remember as an interesting cultural aspect of communication. Once again, I would like to thank the committee for the helpful comments and suggestions while creating this thesis.

Finally, I would like to express my gratitude to all the people and study colleagues I met during the past years in Athens, who turned my stay into an impressively rich and interesting experience. And, of course, I would like to thank my parents, Christine and Tom, who supported me over this long distance and through my entire life.

Contents

List of Figures

List of Tables

Chapter 1

Introduction

Multidisciplinary research has intensified in recent years to investigate fundamental folding mechanisms of polymers. The biological function of biopolymers and large proteins in particular, is dominated by the geometrical structure. Folding and unfolding are natural processes under biological conditions. However, misfolding can cause illnesses or severe diseases. A proper understanding of folding pathways from a functional to a dysfunctional state in a complex biological environment is vital for the development of proper treatment, drug design and drug delivery. Recently, graphene sheets were suggested as a potential substrate for medical substances [1]. Also, the fabrication of bioelectrocatalysts on carbon nanotubes [2] and the construction of light switches on graphene based transistors [3] are further examples where adhesion enhancement of polymers [4, 5] on graphene sheets plays an important role.

Apart from biological systems, adsorbed polymers are commonly utilized in the assembly of novel two dimensional nanomaterials [6]. A key element in the development and enhancement of electronic applications like photovoltaics or field-effect transistors (FETs) is the manipulation of the electronic band structure. Transition metal dichalcogenides (TMX_2) and metal monochalcogenides (MX) were identified as suitable classes of materials. Recently, research interests were focused on MoS_2 or GaSe, which show hexagonal symmetry. These

materials allow for band gap engineering, but are in general not chemically inert. Thus, polymer films are explored to serve as protective coatings and to mechanically stabilize these thin materials on solid substrates [7, 8] and in liquid solutions [6]. The given examples illustrate the wide range where polymer-surface interactions are relevant. Although different polymers and substrate materials are already used for specific purposes, general adsorption mechanisms and thermodynamics are not yet understood. Therefore, a systematic but general investigation of polymer adsorption effects on substrates is necessary.

The goal of this study is to understand the cooperative behavior of structure formation processes in a *complex system*. A physical system is considered to be complex if its constituents interact and exhibit multiple degrees of freedom. This work examines the *cooperativity* of a semi-classical polymer system, which means that mutual, simultaneous and hierarchical many-body interactions can impose a higher order and hence reduce entropy. Further, structural phases of the system and transitions between them are analyzed. A *conformational phase* characterizes the system subject to environmental constraints, where the majority of configurations share similar physical properties. Generally, phase transitions are the discernible result of competing, internal energetic and entropic effects which are influenced by external environmental parameters like temperature, pressure, chemical potential etc.

For macromolecular systems, one important parameter is the temperature. At high temperatures molecules show generally gas-like, extended random-coil phases which collapse towards lower temperatures into liquid-like globular phases. If the temperature is decreased further, the system's constituents arrange ultimately in crystalline or amorphous structures. Although this coarse scheme of structural phase transitions applies to macromolecular systems in general, subphases of different geometrical shape and changes in the location of phase transitions arise from the specifics of the system under consideration. Such irregular thermodynamic behavior can be induced, for example, by surface effects and discrete sym-

metries due to the finite size of the polymer [9]. In this context the adsorption of polymers to nanowires and nanocylinders has been investigated [10, 11]. Further simulations were performed to study the adsorption to flexible membranes [12] and the effect of attractive stripe-like surface patterns [13].

In this thesis discrete attraction sites on a hexagonal substrate are considered. A surface adsorption strength parameter is used to determine how the structural response and cooperativity of the polymer system depends on intramolecular or monomer-substrate interactions. To provide the reader with a complete overview of the computational approach to address these questions, the thermodynamics and statistical mechanics, which form the basis for the simulation of polymer systems, are summarized in Chapter 2. With the theoretical background at hand, the coarse-grained model for an elastic, flexible homopolymer is developed in Chapter 3. In this chapter one specific parametrization is selected for the bonded FENE and Lennard-Jones interaction, following the publication [14]. Next, the computational methodology is presented in Chapter 4, where the parallel tempering method is discussed and details of the implementation are described, as published in [15]. Thermodynamic results, together with a discussion of the 16 observed structural phases are provided in Chapter 5. Observed phases are compared between different system sizes and substrates, following the publication [16]. Additionally, a complete structural hyperphase diagram is presented for a 55mer and details of the pattern recognition process are discussed. The conclusion of this study is provided in Chapter 6 together with an outlook on novel questions which arise from the results of this research.

Chapter 2

Thermodynamics and statistical mechanics

Thermodynamics describes the behavior of many particles in a thermodynamic environment, for example a heat bath. As an empirical theory it introduces macroscopic quantities for large system sizes where microscopic fluctuations are averaged out. Resulting macrostates are governed by the thermodynamic laws. Phase transitions can be found for interacting systems. Different types of phase transitions are typically distinguished by means of discontinuities in the derivatives of suitable thermodynamic potentials as functions of their natural variables, for example the Helmholtz free energy $F(T, V, N)$ or the Gibbs free energy $G(T, P, N)$, which is denoted as *Ehrenfest's classification*.

Important to the results presented in this work are first and second order phase transitions. Transitions of second order show continuous behavior in the first derivative and a discontinuity in the second derivative of the free energy with respect to a thermodynamic variable. For instance, the specific heat $C_V/N \propto (\partial^2 F(T, V, N)/\partial T^2)_{V,N}$ exhibits a discontinuity at the critical temperature. At a second order phase transition universal critical properties can be found such as the divergence of the correlation length, allowing for scale

freedom. For studies of various finite systems this scaling hypothesis is exploited by the application of finite size scaling. In the study at hand the scale freedom close to second order phase transitions is one argument to motivate our coarse-grained approach, introduced in Chapter 3, and explains the general nature of the obtained results.

2.1 The free energy

A canonical analysis is typically the starting point for the investigation of polymer systems, where the number of particles N, volume V and temperature T are easily accessible control parameters. Associated with these variables is the free energy,

$$F(T, V, N) = U(S, V, N) - T\ S(T, V, N), \tag{2.1}$$

which incorporates the internal energy U and the entropy S. It is important to note that for a system embedded into a heat bath the free energy is minimal at equilibrium. Therefore, the equilibrium state of a physical system can be examined by analyzing this thermodynamic potential with respect to order parameters, which is typically denoted as a free-energy landscape. Crucial in this context is the development of phase specific order parameters as discussed in Chapter 5.

2.2 Statistical ensembles

Although thermodynamics can describe the cooperative behavior of systems in the thermodynamic limit, an understanding of the cooperativity, especially in systems of finite size, can only be based on the fundamental processes which involve thermal fluctuations of microscopic degrees of freedom. The computational methodology to simulate these fluctuations on

computers will be explained in chapter 4. The occurrence of microstates subject to environmental constraints is governed by the concept of statistical ensembles.

2.2.1 The microcanonical NVE ensemble

The simplest ensemble is the closed system where the number of particles N, the volume V and the energy E are kept constant. Since every measurement will be of finite accuracy, a very sharp interval $\delta E \ll E$ is typically considered. The number of accessible microstates with energy E_i is therefore defined as

$$\Omega(E) = \sum_{E-\delta E/2<E_i<E+\delta E/2} 1. \tag{2.2}$$

Since no state is distinguished by a certain macroscopic property it is postulated that each microstate i occurs with the same probability

$$p_{\mathrm{mic}}(E_i) = \begin{cases} \frac{1}{\Omega(E)}, & E - \delta E/2 < E_i < E + \delta E/2, \\ 0, & \text{otherwise} \end{cases} \tag{2.3}$$

Finally, the thermodynamic quantities entropy and temperature are defined as system properties which depend on the parameter E,

$$S = k_B \ln \Omega(E), \tag{2.4}$$

$$\frac{1}{T} = \frac{\partial S(E)}{\partial E}. \tag{2.5}$$

The significance of expression (2.4) lies in the connection of microscopic statistics with macroscopic thermodynamics.

2.2.2 The canonical NVT ensemble and the Boltzmann factor

Experimentally more easily accessible is the canonical ensemble where the temperature is considered as an external parameter. For macroscopic systems the temperature can be controlled by a large heat bath. The probability distribution of microstates is typically motivated by considering both, the system of interest and the heat bath to be a microcanonical ensemble with energy $E = E_i + E_{\text{bath}}$. It is considered that the system and the much larger heat bath ($E_i \ll E_{\text{bath}}$) are in thermal equilibrium and weakly interacting.

The accessible microstates of the combined system $\Omega(E)$ are equally probable. If in a discrete system the microstate i of the system is fixed, the remaining $\Omega_{\text{bath}}(E - E_i)$ states of the heat bath are still equally distributed. The probability to find the system in the i^{th} state is expressed by the ratio of states of the heat bath and the total number of states,

$$p_{\text{can}}(E_i; T) = \frac{\Omega_{\text{Bath}}(E - E_i)}{\Omega(E)}. \tag{2.6}$$

Now the entropy of the bath is expanded in a Taylor series, where terms of order $\mathcal{O}(E_i^2)$ and higher are truncated and the definition of the microcanonical temperature (2.5) is inserted,

$$\begin{aligned} k_{\text{B}} \ln \Omega_{\text{Bath}}(E - E_i) &= k_{\text{B}} \ln \Omega_{\text{Bath}}(E) - k_{\text{B}} \frac{\partial \ln \Omega_{\text{Bath}}(E)}{\partial E} E_i + ... \\ &= k_{\text{B}} \ln \Omega_{\text{Bath}}(E) - \frac{E_i}{T} + ... \end{aligned} \tag{2.7}$$

Neglecting higher order terms, the last expression is substituted into (2.6) and yields the canonical microstate probability,

$$p_{\text{can}}(E_i; T) = \underbrace{\frac{\Omega_{\text{Bath}}(E)}{\Omega(E)}}_{1/Z} \; e^{-\frac{E_i}{k_{\text{B}} T}}. \tag{2.8}$$

The partition function Z was introduced as the normalization factor of the canonical probability and is therefore calculated by the summation over all microstates,

$$Z(T) = \sum_i e^{-\frac{E_i}{k_\mathrm{B}T}}. \tag{2.9}$$

However, this physically motivated derivation does not directly provide a connection to thermodynamic quantities. Mathematically more compact but without consideration of the physical limitations, the canonical microstate probability $p_\mathrm{can}(E_i;T) = p_i$ can be obtained by the maximization of information entropy $S_I = -\sum_i p_i \ln p_i$ [17, 18], using Lagrange multipliers which incorporate the constraints normalization and average energy,

$$\begin{aligned} 0 &= \delta \left\{ \sum_i p_i \ln p_i + \alpha \left(\sum_i p_i - 1 \right) + \beta \left(\sum_i p_i E_i - \langle E \rangle \right) \right\} \\ &= \sum_i \delta p_i \left(\ln p_i + 1 + \alpha + \beta E_i \right) \quad \Rightarrow \quad p_i = \underbrace{e^{-1-\alpha}}_{1/Z} \, e^{-\beta E_i}. \end{aligned} \tag{2.10}$$

This result yields an expression for the information entropy which describes the disorder in the system,

$$S_I = -\frac{1}{Z} \sum_i e^{-\beta E_i} \ \ln \frac{e^{-\beta E_i}}{Z} = \ln Z + \beta U. \tag{2.11}$$

Inserting the Boltzmann constant in this expression, $k_\mathrm{B}\ S_I = S$ is identified with the thermodynamic entropy. By comparison with (2.1) the relation between free energy and the partition function follows as

$$F = -k_B T \ \ln Z, \tag{2.12}$$

where the inverse thermal energy is associated with the Lagrange multiplier $\beta = 1/(k_\mathrm{B}T)$. Traditionally, the partition function is described as a generating function, as it governs all

physical behavior. Once the functional form of the partition function is obtained, thermodynamic quantities of interest can be calculated from its temperature derivatives. Using computer simulations, however, the partition function is difficult to obtain directly, since it requires the summation over all microstates.

The number of microstates is unknown, so that a cutoff energy for states that need to be sampled for a given temperature can hardly be determined. However, the number of microstates in the infinitesimal interval $\mathrm{d}E$ defines the density of states $g(E)$ where the energy is a continuous parameter. In computer simulations a relative estimate for $g(E)$ is determined for a finite energy bin δE. In Chapter 4.3 the estimation technique for the density of states by means of multiple histogram reweighting is discussed, starting from the canonical energy distribution

$$P_{\mathrm{can}}(E;T) = \frac{1}{Z}\, g(E) e^{-\frac{E}{k_{\mathrm{B}}T}}. \tag{2.13}$$

The exponential term to the right is referred to as the *Boltzmann factor* and describes the exponential decay of the probability density to find a populated state at energy E.[a] The Boltzmann factor in (2.13) is multiplied by the density of states which is increasing for typical polymer systems in the regime of interest, leading to a Gaussian shape of the canonical distribution. In the case of a first-order transition, phases of different energy coexist, while in a finite system states with an intermediate energy are entropically suppressed. This leads to a *convex intruder* in the density of states and in the entropy. As a result, the canonical distribution energy becomes bimodal.

[a] Generally, if the given *extensive quantities* of the microcanonical ensemble are replaced by constraints on *intensive quantities*, then exponential terms in the probability distribution, similar to the Boltzmann factor are created by the average value of the replaced extensive quantities, cf. (2.10)

Integration of the density of states over the very small energy interval, $\Omega(E) = g(E)\delta E$, provides the connection to the microcanonical entropy (2.4) as the thermodynamic function of choice,

$$S(E) = k_\mathrm{B} \ln g(E) + k_\mathrm{B} \ln \delta E \qquad \Rightarrow \qquad S(E) \propto k_\mathrm{B} \ln g(E). \tag{2.14}$$

Since microcanonical analysis only requires derivatives of the entropy, the constant term as well as the unit inside the logarithm is dropped. For convenience, the Boltzmann constant is set to unity in the following.

2.3 Temperature derivatives and fluctuations

Temperature derivatives of structural and energetic quantities describe the response of the system to a change in temperature and can signal structural phase transitions. The mean value of any energetic quantity $O(E)$ follows from (2.13) as

$$\langle O \rangle(T) = \frac{\int \mathrm{d}E \; O(E) \; g(E) \; e^{-\beta E}}{\int \mathrm{d}E \; g(E) \; e^{-\beta E}}, \tag{2.15}$$

The temperature derivative leads to the covariance between the quantity and the energy,

$$\begin{aligned} \frac{\mathrm{d}\langle O \rangle(T)}{\mathrm{d}T} &= \frac{\int \mathrm{d}E \; O(E) \; E \; g(E) \; e^{-\beta E}}{k_\mathrm{B} T^2 \int \mathrm{d}E \; g(E) \; e^{-\beta E}} - \frac{\int \mathrm{d}E \; O(E) \; g(E) e^{-\beta E} \times \int \mathrm{d}E \; E \; g(E) \; e^{-\beta E}}{k_\mathrm{B} T^2 \left(\int \mathrm{d}E \; g(E) \; e^{-\beta E} \right)^2} \\ &= \frac{\langle O \; E \rangle - \langle O \rangle \; \langle E \rangle}{k_\mathrm{B} T^2} \; . \end{aligned} \tag{2.16}$$

Microscopic fluctuations in the canonical ensemble, which are measured in the simulation, are with (2.16) directly related to the corresponding response quantity.

2.4 Configurational thermodynamic quantities

For an *ergodic system* of N interacting particles with Hamiltonian $H(\{q_\nu, p_\nu\}) = H(\gamma)$ the mean kinetic energy is proportional to the temperature. To show this, the flowing general expression

$$\left\langle \gamma_i \, \frac{\partial H}{\partial \gamma_j} \right\rangle = \frac{\int \gamma_i \frac{\partial H}{\partial \gamma_j} \, e^{-\beta H} \, \mathrm{d}^{6N}\gamma}{\int e^{-\beta H} \, \mathrm{d}^{6N}\gamma}, \tag{2.17}$$

is evaluated, where $\gamma \in \Gamma$ denotes a point in the 6N dimensional phase space Γ, spanned by the components of generalized coordinates q_ν and canonical momenta p_ν. Noticing a simple integration rule for the γ_j component of the phase space variable

$$\frac{\partial}{\partial \gamma_j} \, e^{-\beta H} = -\beta \, \frac{\partial H}{\partial \gamma_j} \, e^{-\beta H} \qquad \Rightarrow \qquad \int \frac{\partial H}{\partial \gamma_j} \, e^{-\beta H} \mathrm{d}\gamma_j = \frac{-1}{\beta} e^{-\beta H}, \tag{2.18}$$

integration by parts is applied to the j^{th} component of the first integral in (2.17) which yields

$$\left\langle \gamma_i \, \frac{\partial H}{\partial \gamma_j} \right\rangle = \frac{\int \gamma_i \left(\frac{-1}{\beta} e^{-\beta H} \right) \, \mathrm{d}^{6N-1}\gamma \Big|_{\gamma_j=\gamma_-}^{\gamma_j=\gamma_+} - \int \frac{\partial \gamma_i}{\partial \gamma_j} \left(\frac{-1}{\beta} e^{-\beta H} \right) \, \mathrm{d}^{6N}\gamma}{\int e^{-\beta H} \, \mathrm{d}^{6N}\gamma} = \frac{\delta_{ij}}{\beta} = \delta_{ij} \, k_{\mathrm{B}} T. \tag{2.19}$$

The first term in the nominator vanishes due to the character of the extremal values $\gamma_\pm$. If γ_j represents a component of a momentum these are $\gamma_\pm = p_{\nu,\pm} = \pm\infty$; otherwise if γ_j stands for the spatial coordinate the boundary value coincides with the location of the walls of the container $\gamma_\pm = q_{\nu,\pm} = q_{\text{wall},\pm}$, since the volume is considered finite. In both cases the

Hamiltonian diverges so that the integrand becomes zero. Eq. (2.19) is used to evaluate the average kinetic energy of a particle system in a canonical ensemble

$$\langle E_{\text{kin}} \rangle = \frac{1}{2} \sum_{\nu=1}^{3N} \left\langle p_\nu \, \frac{\partial H}{\partial p_\nu} \right\rangle = \frac{3}{2} N k_B T \qquad \text{[b]}. \tag{2.20}$$

If the potential depends on the location of all interacting particles in the configuration $\mathbf{X} = (\vec{r}_1, ..., \vec{r}_N)$ the mean value of the total energy is written as,

$$\langle H \rangle = \frac{3}{2} N k_B T + \langle U(\mathbf{X}) \rangle. \tag{2.22}$$

The total heat capacity of the system $\tilde{C}_V$ follows as temperature derivative of the heat Q,

$$\tilde{C}_V = \left(\frac{\delta Q}{\delta T} \right)_V = \left(\frac{\partial \langle H \rangle}{\partial T} \right)_V = \frac{3}{2} N k_{\text{B}} + \underbrace{\frac{1}{k_{\text{B}} T^2} \left(\langle U^2(\mathbf{X}) \rangle(T) - \langle U(\mathbf{X}) \rangle^2(T) \right)}_{\text{configurational heat capacity } C_V}. \tag{2.23}$$

Since the first term in the specific heat, which arises from the kinetic energy of the particles, is constant, all signals associated with phase transitions are encoded in the fluctuation of the potential energy U, which is for simplicity typically denoted as the energy of the configuration $E(\mathbf{X})$. In the following discussion, only the configurational heat capacity C_V is considered. Analogously, all system properties are governed by the *configurational density of states*, and we redefine $g(E)$ as,

$$g(E) = \int \mathcal{D}\mathbf{X} \, \delta \left(U(\mathbf{X}) - E \right). \tag{2.24}$$

[b] The same result as in (2.20) is found for the average potential energy if particles are non-interacting and in an external harmonic potential, known as the *equipartition theorem*

$$\langle V \rangle = \frac{1}{2} \sum_{\nu=1}^{3N} \left\langle q_\nu \, \frac{\partial H}{\partial q_\nu} \right\rangle = \frac{1}{2} \sum_{i=1}^{N} \langle \vec{r}_i \, \nabla_{\vec{r}_i} U \rangle = \frac{3}{2} N k_B T. \tag{2.21}$$

Chapter 3

Model for an elastic, flexible homopolymer grafted on a hexagonal surface

3.1 Motivation of the coarse-grained approach

Polymers are macromolecules which incorporate a vast amount of atoms in a chain-like structure of repeated chemical groups or side chains. Proteins are complex, biologically functional examples which involve on the order of 10^5 atoms. These objects were found by nature during an evolutionary process but it is not yet understood how specific sequences in a biological environment close to room temperature can fold into a functional structure. However, it is known that the geometric structure of a protein is the key element to a specific function.

The structure formation process of polymer chains is a cooperative process of many interacting parts of the system. However, the overall behavior does not necessarily depend

on atomistic details which motivates the concept that single chemical groups act like a coarse-grained entity and can be represented by one interacting particle denoted as a polymer bead or monomer.

Especially the physical properties of second-order phase transitions justify the coarse-grained approach to the analysis of structure formation and structural phases. The critical behavior at second-order phase transitions is associated with the divergence of the correlation length. Microscopic details become negligible and the system is maximally cooperative. Therefore, different systems exhibit the same universal behavior. Finally, a coarse-grained model captures the physical essence of phase and structure formation processes.

3.2 The non-bonded, intramolecular interaction

Essential to any cooperativity is the many-body interaction between non-bonded polymer beads. In this study the structure formation of an uncharged chain of the same repeating unit denoted as a flexible homopolymer [19–21] is investigated where one end of the chain is grafted to an infinitely large hexagonal substrate.

The attractive interaction between non-bonded beads separated by the distance r is described by the London dispersion force [22–24]. It is part of the Van-der-Waals force and originates from the Coulomb interaction between residual dipoles of the two monomers interacting with each other. Spontaneous charge fluctuations are treated in a multipole expansion where the leading dipole term creates a $1/r^3$ dependence in the attractive potential. Quantum-mechanical calculations in second-order perturbation theory show that the electronic fluctuations reduce the range of the interaction to a $1/r^6$ potential.

Coulomb repulsion and Pauli exclusion become apparent if beads come close to each other. For mathematical simplicity a repulsive term with $1/r^{12}$ dependence was introduced by Lennard-Jones [25] leading to the famous potential of the form

$$U_{LJ}(r) = 4\varepsilon \left[\left(\frac{\sigma}{r}\right)^{12} - \left(\frac{\sigma}{r}\right)^{6} \right], \tag{3.1}$$

which accurately describes the interaction of noble gases [26] and approximates well potentials between other atoms and molecules. The material dependent parameter is with $\sigma = 2\, r_{\mathrm{VdW}}$ related to the Van-der-Waals radius of the particles which is the minimum distance between particles that approach each other from an infinitely large distance without any initial energy.

In the simulation the energy scale $\varepsilon \equiv 1$ as well as the minimum location of the potential $r_0 = 2^{1/6}\sigma \equiv 1$. Based on this definition we present all results on energetic scales of ε and length scales of r_0. Accordingly, temperatures are stated in units of $\varepsilon/k_{\mathrm{B}}$. In order to avoid the computationally expensive calculation of weak long-range interactions, the Lennard-Jones potential is truncated at the cutoff distance $r_{\mathrm{c}} = 5\sigma/2$ and shifted by $U_{\mathrm{shift}} = U_{\mathrm{LJ}}(r_{\mathrm{c}})$, resulting in the potential for the non-bonded interaction,

$$U_{\mathrm{NB}}(r) = \begin{cases} U_{\mathrm{LJ}}(r) - U_{\mathrm{shift}}, & r < r_{\mathrm{c}}, \\ 0, & \text{otherwise.} \end{cases} \tag{3.2}$$

3.3 The interaction of bonded monomers

Covalent bonds show for small deviations from their equilibrium length harmonic behavior. For larger extension these bonds become rather stiff. Therefore, the interaction of bonded monomers is modeled by the finitely extensible nonlinear elastic (FENE) potential [27–29], given in the first term,

$$U_{\mathrm{B}}(r) = -\frac{1}{2} K R^2 \ln\left[1 - \left(\frac{r - r_0}{R}\right)^2\right] + \eta(U_{\mathrm{LJ}}(r) + \varepsilon) - \varepsilon - U_{\mathrm{shift}}, \tag{3.3}$$

where a Lennard-Jones potential is added to account for volume exclusion due to polarization effects. The stiffness of the FENE bond, controlled by the parameter $R \equiv 3/7$, and the spring constant $K \equiv 98/5$ are set to standard values. The logarithmic form of the FENE potential restricts the bond length to the interval $r \in [r_0 - R, r_0 + R]$, where the equilibrium bond length r_0 is chosen to coincide with the location of the potential minimum of the non-bonded interaction (3.2).

Different polymer models have been investigated, where the bond between adjacent monomers is only based on the FENE potential [30–32] and where an additional Lennard-Jones interaction was considered [33–35]. Here, the additional Lennard-Jones term in (3.3) is controlled by the parameter η which introduces asymmetry to the potential of the polymer bond. In Ref. [14] we have shown that this parameter influences the strength of the freezing transition and the geometrical shape of the ground-state structure. For typical values such as $\eta = 1$ the frozen phase of a polymer with $N = 55$ monomers reveals an icosahedral shape, as it is discussed in detail in section 5.2.1. The solid-like phase is for $\eta \geq 0.04$ separated by a first-order-like transition from the liquid-like phase. For smaller values the order of the transition is reduced gradually to a fourth-order transition [14] in the case of $\eta = 0$, where a bihexagonal ground state conformation is found.

Besides the interesting change in the structural behavior due to altered values of the η parameter, the change in the order of the freezing transition has also a crucial technical consequence: The efficiency of the parallel tempering method, described in section 4.2, drops rapidly near strong first-order transitions. Therefore, reduced values of η can make the model computationally less challenging. However, in order to retain the overall behavior of standard models the asymmetry parameter was set to $\eta = 0.1$ in this study, see Fig. 3.1.

Deviations from the optimal bond length cause an energy penalty. In order to prepare the discussion of bond length distributions it is useful to introduce a modified bonded potential which discriminates compressed and stretched bonds,

$$U_{\mathrm{B}}^{(\mathrm{mod})}(r) = \mathrm{sign}(r - r_0)\ \left(U_{\mathrm{B}}(r) + \varepsilon + U_{\mathrm{shift}}\right). \tag{3.4}$$

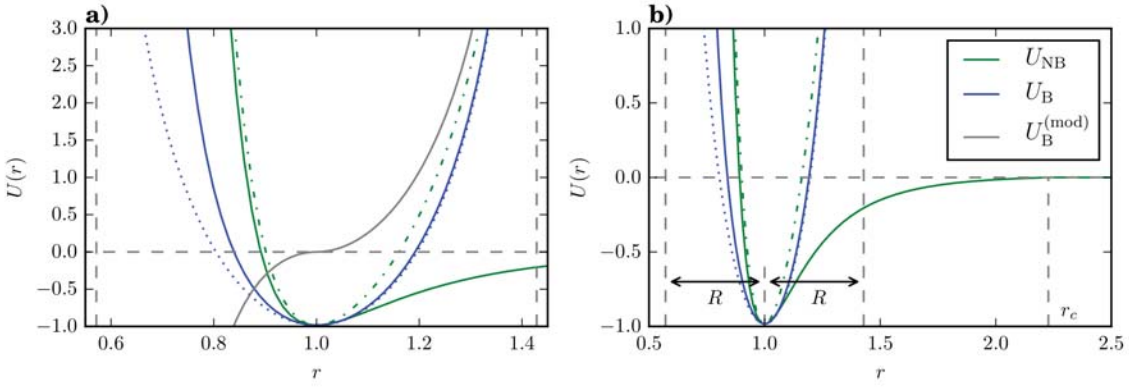

Figure 3.1: The potentials of the non-bonded and bonded interactions $U_{\mathrm{NB}}(r)$ and $U_{\mathrm{B}}(r)$, respectively, are shown as functions of the monomer-monomer distance r, on different scales in a) and b). For the bonded potential the asymmetry parameter, introduced in (3.3), is set to $\eta = 0.1$. To illustrate its effect on the repulsive flank the bonded potential is also shown for $\eta = 0.0$ (dotted) and $\eta = 1.0$ (dot-dashed). The modified bonded potential $U_{\mathrm{B}}^{(\mathrm{mod})}(r)$, given in (3.4), is depicted in panel a) by a gray solid line.

3.4 The monomer-surface interaction

The interaction between polymer beads and surface vertices is governed by the same effects as the intramolecular non-bonded potential. In order to allow for implicit solvents surrounding the polymer and different hexagonal surface materials, the adsorption strength parameter ε_S is introduced in the potential of the interaction between a single lattice vertex and a monomer at distance r,

$$U_{\mathrm{S}}(r) = \varepsilon_{\mathrm{S}}\, U_{\mathrm{NB}}(r), \tag{3.5}$$

where the same cutoff value is chosen as in the non-bonded case. The key question in this study is how the polymer behavior depends on adsorption strength and which structural phases can be observed. Hence, the adsorption strength parameter is changed for independent simulations in the interval $\varepsilon_{\mathrm{S}} \in [0.0, 5.0]$. In Fig. 3.2 the interactions introduced here are illustrated. Parameter values of the potentials are summarized in Tab. 3.1. The total energy of a conformation $\mathbf{X} = (\vec{r}_1, \ldots, \vec{r}_N)$ is given by

$$E(\mathbf{X}) = \sum_{i=1}^{N-2} \sum_{j=i+2}^{N} U_{\mathrm{NB}}(r_{ij}) + \sum_{i=1}^{N-1} U_{\mathrm{B}}(r_{ii+1}) + \sum_{i=2}^{N} \sum_{a=1}^{\infty} U_{\mathrm{S}}(r_{ia}), \tag{3.6}$$

where the monomer-monomer distance is $r_{ij} = |\vec{r}_i - \vec{r}_j|$ and $r_{ia} = |\vec{r}_i - \vec{s}_a|$ is the distance between a monomer i and a surface vertex a. Although surface and non-bonded interactions are both described by a Lennard-Jones potential, which is well studied for different polymer systems, novel structure formation processes and undiscovered structural phases are expected to arise from the hexagonal pattern of the substrate. In order to understand the driving forces behind the polymer adsorption process the three-dimensional potential landscape of the substrate is investigated next.

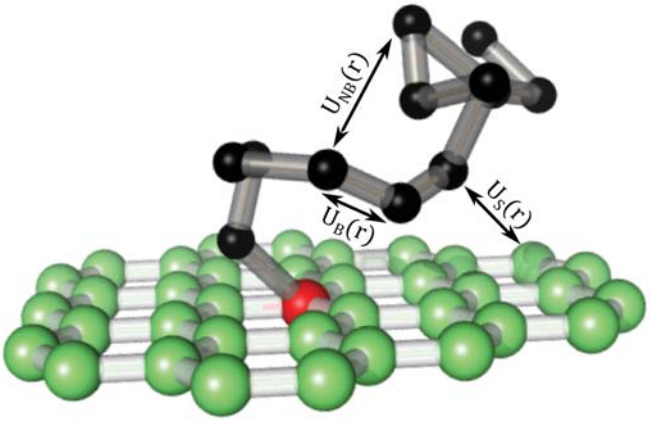

Table 3.1: Potential parameters

potential	parameter	value
$U_B(r)$	$K = 98/5$	19.600
	$R = 3/7$	0.4296
	$r_0 = 1$	1.0000
	$\eta = 1/10$	0.1000
$U_{NB}(r)$	$\varepsilon = 1$	1.0000
	$\sigma = r_0/2^{1/6}$	0.8911
	$r_c = 5\sigma/2$	2.2275
$U_S(r)$	$\varepsilon_S \in [0, 5]$	variable

Figure 3.2: The different interaction types of monomers are depicted for a typical conformation of a 13mer. The chain of polymer beads (black) is grafted with the first monomer (red) on a infinitely large, fixed, hexagonal surface. Selected surface vertices (green) in proximity to the first monomer are depicted. The potential $U_B(r)$ defined in (3.3), describes the interaction of two subsequent monomers which are connected by a modified FENE bond (gray). The interaction of non-bonded polymer beads is governed by a modified Lennard-Jones potential (3.2). Monomer and surface vertices interact via the surface potential U_S given in (3.5). Parameter definitions and values for the different potentials are summarized in the Table 3.1.

The combined effective surface potential of all lattice sites in the plane $z = 0$

$$U_{\mathrm{S,c}}(x, y, z) = \sum_{a=1}^{\infty} U_{\mathrm{S}}(|\vec{r} - \vec{r}_a|) \tag{3.7}$$

is presented along different Cartesian coordinates. The hexagonal pattern is apparent in Fig. 3.3 a) where the surface is viewed from the top. Values of the surface potential at a height $z = 0.81$ are indicated by color. Orange dots mark high potential values due to repulsion from the underlying substrate vertices. Black color indicates locations where the potential is minimal, and monomers are expected to reside. The two perpendicular black lines mark vertical cuts of the potential. These vertical cuts are depicted in Fig. 3.3 c) and d). The brown semi-spherical shapes mark the areas which are forbidden for a monomer

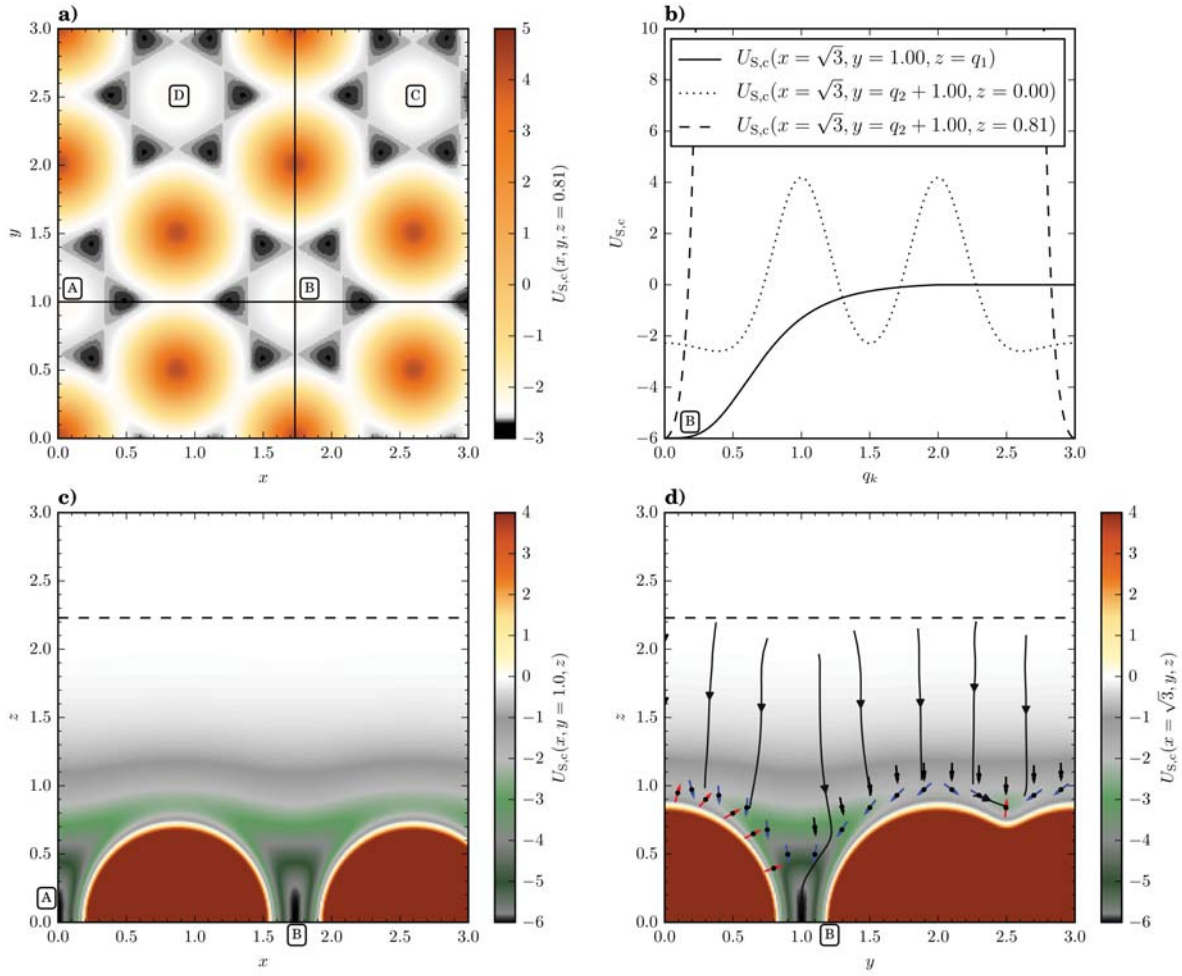

Figure 3.3: The combined surface potential $U_{\mathrm{S,c}}(x, y, z)$ of vertices in a hexagonal lattice, defined in (3.7), is shown from the top in the density plot a) at $z = 0.81$. The locations of hexagonal centers are labeled from A-D. In graph b) the potential is shown as function of the distance measured from the center of a hexagonal ring, in vertical direction $q_1 = z$ (solid line) and parallel to the y axis, as function of $q_2 = y + 1.00$ (dashed line). For the latter parameter the potential is also given at the height $z = 0.81$ above the surface (dotted line). A side-view of the potential is displayed along two cuts $y = 1.00$ c) and $x = \sqrt{3}$ d), where the potential minima A and B are indicated by black color. In panel d) field lines (black) tangential to the gradient of the potential (red, blue and black arrows, length normalized) are superimposed.

due to volume exclusion. This area is confined by a white line where the potential $U_{\mathrm{S,c}}(x, y, z) = 0$. Monomers of the polymer typically reside above this equipotential surface which is plotted three-dimensionally in Fig. 3.4.

Recall that a monomer is represented as a point in this effective representation of the potential. Returning to Fig. 3.3 a), the cut in the x-direction intersects two hexagonal centers, labeled by A and B. Therefore, the attractive centers inside a hexagonal ring are found in panel c) for $z = 0$ at $x = 0, \sqrt{3}$. Similarly, minimum B is shown from a different perspective in d) at $y = 1$.

In order to indicate the path which a slow particle would follow at $T = 0$, field lines are superimposed. These field lines are tangential to the negative gradient of the combined potential, marked by arrows. For heights $z > 1.3$ trajectories point almost perpendicularly towards the surface. Below this value monomers are primarily attracted by the closest lattice vertex, before the field lines bend at distances sightly larger than the Van-der-Waals radius towards a potential minimum. One representative field line ends at $y = 1$ in a hexagonal center. Note, that field lines which seem to end in a local valley at $y = 2.5$ continue above or below the paper plane towards a hexagonal center (at $x = \sqrt{3}/2$ and $x = 3\sqrt{3}/2$), apparent in the three-dimensional plot in Fig. 3.4.

In panel c) and d) we observe that the minima inside hexagonal rings are confined in the lateral directions but extends up to about $z < 0.2$ into the vertical direction. Fig. 3.3 b) provides one-dimensional graphs to quantify this statement. The solid line shows the surface potential as a function of height, where the dashed line is the potential in y direction, starting in each case from the minimum location given in Fig. 3.3 d). Analogously, the third dotted line indicates the potential along the y-direction, but at the height $z = 0.81$ above the surface plane. The two peaks in the potential arise from the cut through the semi-spherical area of repulsion in Fig. 3.3. Note, that the radius of the semi-spheres in panel c) is larger than in d), since for the latter case the depicted plane cuts through substrate vertices.

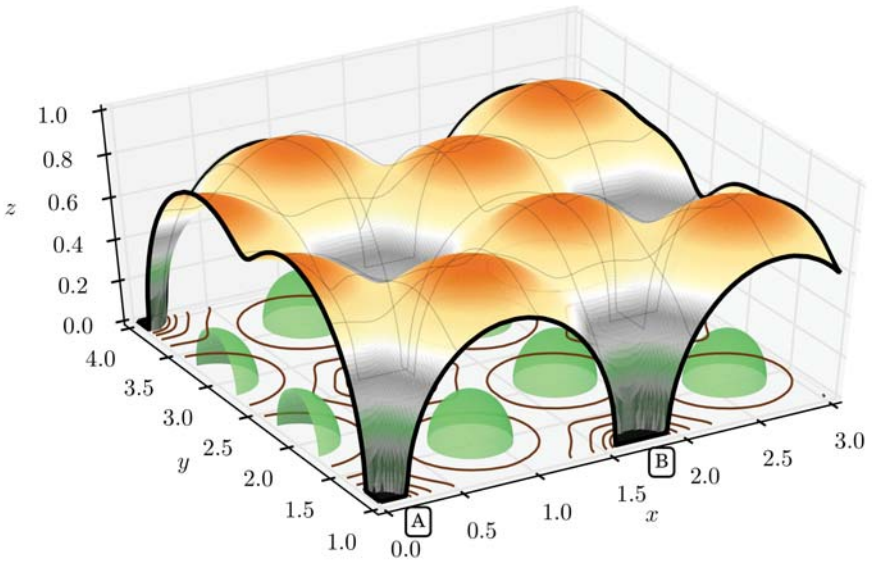

Figure 3.4: The equipotential surface $U_{\mathrm{S,c}}(x, y, z) = 0$ is shown where the surface cut along the x and y direction can be identified with the white line in Fig. 3.3 c) and d), respectively. Monomers of the homopolymer reside above this surface. The height is indicated by color. Green hemispheres indicate the vertices of the hexagonal substrate, as shown in Fig. 3.2. The potential minima, located in the center of the hexagonal substrates are labeled by A and B along the x axis, c.f Fig. 3.3 c).

This detailed discussion of the surface potential provides insight into the behavior of the polymer at low temperatures, where entropic effects in the free-energy landscape play a negligible role. A polymer bead favorably resides in the centers of hexagonal rings. However, the finite character of the bond does not allow placing two adjacent monomers into neighboring hexagonal centers. Instead, depending on the adsorption strength, one or more additional linking monomers are required in between. These linking monomers reside above the surface depicted in Fig. 3.4. At higher temperatures entropic contributions become important. In order to understand the adsorption process at nonzero temperatures it is therefore necessary to sample and investigate the state space of the homopolymer.

Chapter 4

Computational methodology and implementation

The computational approach towards polymer adsorption on substrate surfaces can be classified in terms of the two distinct, but well-known methodologies, molecular dynamics (MD) and Monte Carlo simulation (MC). In this study a Monte Carlo method was applied that aims directly at the sampling of independent, uncorrelated states of the system subject to thermodynamic constraints without sampling an environment such as a surrounding solvent. Instead, mechanisms to obtain proper statistical ensembles form the foundation of sampling algorithms. The Metropolis algorithm [45] is the most prominent example. In combination with proper Monte Carlo updates, which obey detailed balance, the Metropolis algorithm is designed to obtain configurations in the canonical ensemble. In the context of a system in a thermodynamic environment this corresponds to an NVT ensemble, however, this algorithm can also be used in other contexts like population dynamics. In general, Monte Carlo simulations provide a means to perform integration numerically. Although there are various methods like the trapezoidal rule which converge much more rapidly in one dimension, Monte Carlo simulations are a robust tool that can treat integrals in many dimensions.

Hence, Monte Carlo simulations are suitable to investigate the highly dimensional space of the different degrees of freedom of a homopolymer in order to calculate important quantities like the density of states (2.24).

4.1 Detailed Balance and the Metropolis rule

In Metropolis sampling a new state is proposed based on the previous state, leading to a random walk in state space. Hence, Metropolis sampling is an instance of a Markov chain Monte Carlo method where the probability P_i to sample a state i at the discrete time step t is governed by the Master equation,

$$\frac{\Delta P_i(t)}{\Delta t} = \sum_j \left(P_j(t) W_{j\to i} - P_i(t) W_{i\to j} \right). \tag{4.1}$$

$W_{i\to j}$ denotes the transition probability from state i to j. Goal of the simulation is to sample the state space such that the energies of visited states obey the canonical distribution (2.8),

$$\frac{P_j}{P_i} = \frac{P_{\text{can}}(E_j;T)}{P_{\text{can}}(E_i;T)} = e^{-\beta(E_j-E_i)}, \tag{4.2}$$

with $\beta = 1/(k_{\text{B}}T)$. Hence, it is required that probabilities measured in the simulation lose their time dependence and become stationary, i.e., the right-hand side in (4.1) must vanish. Often it is practical to demand the stronger condition of detailed balance,

$$P_j \, W_{j\to i} = P_i \, W_{i\to j}. \tag{4.3}$$

In this case, the transition probabilities have to be adjusted accordingly. The probability $W_{i\to j}$ can be understood as a product of the probability to algorithmically propose a Monte Carlo update ($M_{i\to j}$) and to accept ($A_{i\to j}$) the new state. Since in this thesis only simple

displacement updates and rotational pivot updates are considered, $M_{i\to j} = \text{const}$. Therefore, the acceptance ratio is given by the canonical distribution,

$$\frac{A_{i\to j}}{A_{j\to i}} = \frac{W_{i\to j}}{W_{j\to i}} = \frac{P_j}{P_i} = \frac{P_{\text{can}}(E_j;T)}{P_{\text{can}}(E_i;T)} = e^{-\beta(E_j-E_i)}, \tag{4.4}$$

where the detailed balance condition (4.3) and (4.2) was used. The larger value of both acceptance ratios is set to one, which leads to the Metropolis acceptance probability [45],

$$A_{i\to j} = \min\left(e^{-\beta(E_j-E_i)}, 1\right). \tag{4.5}$$

4.2 Parallel tempering (replica-exchange) Monte Carlo

The canonical distribution of states describes the system at one temperature. In order to obtain thermodynamic quantities as functions of temperature multiple simulations are necessary.

At the same time it is usually found that unfavorable large correlations in, for example, the coordinates of the polymer occur at low temperatures where the system is in a frozen, solid-like state. Thus, the state space at low temperatures is investigated comparably slowly. In terms of a polymer system one can visualize a dense, droplet-like conformation where large fluctuations can only occur at the surface of the polymer and global changes are unlikely to happen. One solution to this problem is to introduce changes of temperature in order to melt compact conformations. In the parallel tempering method [36–39] multiple computer threads are utilized for this purpose where many identical systems, denoted as replicas, are simulated at the same time but at different temperatures. After sufficiently many Monte Carlo sweeps and measurements, these replicas are exchanged between threads of different

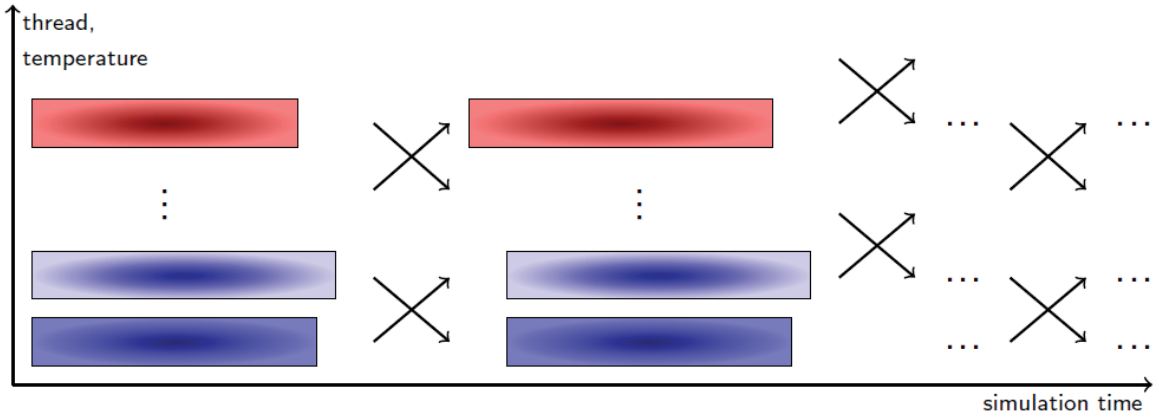

Figure 4.1: Parallel tempering (replica-exchange) scheme, independent simulations of replicas at different temperatures are depicted by colored boxes. Arrows indicate exchanges of replicas between neighboring temperature threads, where exchange partners are alternated.

temperature, see Fig. 4.1. The appropriate number of Monte Carlo steps per monomer (MC sweeps) between exchanges depends on the autocorrleation time of the quantity of interest and on the size of the studied system. In order to fulfill the detailed balance condition, an exchange between replicas at different inverse temperature β has to be accepted according to the Metropolis rule. As in the previous derivation, the goal is to obtain the canonical energy distribution in each thread. They are stochastically independent so that the joint probability to find state i at T_l and state k at T_h reads according to (2.8) as,

$$P^{(2)}_{\text{can}}\big((E_i;T_l),(E_k;T_h)\big) = \frac{1}{Z_l}\, e^{-\frac{E_i}{k_{\text{B}}T_l}} \times \frac{1}{Z_h} e^{-\frac{E_k}{k_{\text{B}}T_h}} \tag{4.6}$$

The acceptance probability for a replica exchange follows analogously to (4.4) and (4.5),

$$\frac{A_{ik\to ki}}{A_{ki\to ik}} = \frac{e^{-\beta_l E_i - \beta_h E_k}}{e^{-\beta_l E_k - \beta_h E_i}} = e^{-(\beta_l-\beta_h)(E_i-E_k)} \tag{4.7}$$

$$\Rightarrow \qquad A_{ik\to ki} = \min\left(e^{-\Delta\beta\ \Delta E}, 1\right). \tag{4.8}$$

From the previous expression it is found that the acceptance probability for a replica exchange depends on the difference in inverse temperature $\Delta\beta = \beta_l - \beta_h$. In order to facilitate successive exchanges, it is desirable that the exchange rate is fairly constant over a large temperature interval.

Especially at low temperatures, where large correlation times are expected, a high exchange rate is desired. Energy distributions in this region are typically very sharp which prevents large fluctuations of the energy difference, i.e. ΔE in (4.8) is almost constant. Hence $\Delta\beta$ is chosen to be constant as well by distributing simulation threads equally in inverse temperature.

This study was carried out using 35 temperature threads in the interval $T \in [0.18, 1.00]$ and 40 threads linearly distributed in $T \in [1.00, 5.00]$ to allow for a more precise localization of transition signals at high temperatures, which is discussed in Chapter 5. For specific parameter values of the surface adsorption strength, where solid-solid transitions were expected, additional simulations with up to 128 threads were used to sample lower temperatures.

The exchange of replicas was performed using Message Passing Interface (MPI) [46, 47]. The MPI framework offers a large library of routines. In this study it was sufficient to utilize the function `MPI_Sendrecv` to exchange the Cartesian coordinates of each replica and the function `MPI_Gather` to collect output data, where the command `MPI_Type_create_struct` aided to communicate more complex data structures.

4.3 Multiple histogram reweighting

Although simulations were performed at discrete temperatures it is possible to calculate thermodynamic quantities as continuous functions as stated in (2.15). This approach requires the density of states $\hat{g}_E$, here estimated at discrete energy values. Since the canonical histogram $h_{T,E}$ is proportional to the canonical energy distribution (2.13) a relative estimate is calculated by dividing out the Boltzmann factor

$$h_{T,E} = \int_{E-\Delta E/2}^{E+\Delta E/2} d\tilde{E}\ \hat{P}_{\text{can}}(\tilde{E})\ M \quad \Rightarrow\ h_{T,E} \sim \hat{g}_E e^{-\beta E}\ \Delta E\ M, \tag{4.9}$$

$$\Rightarrow \hat{g}_E \sim h_{T,E}\ e^{\beta T}, \tag{4.10}$$

where M denotes the total number of measurements. Note that the density of states is only estimated up to a constant. Therefore, estimates from histograms measured at different temperatures show a parallel shift. Secondly, the statistical error of the histogram depends on the height, such that the variance in height is $\sigma_h \sim 1/\sqrt{h}$. Hence, the estimate for the density of state is most accurate in the energy interval where the histogram is peaked.

The weighted histogram analysis method (WHAM) [40, 41], also known as multiple histogram reweighting, combines the information of histograms obtained at different temperatures T. At each histogram bin, centered around the energy E, $\hat{g}_E$ is estimated, using an initial value for the partition function

$$\hat{g}_E = \frac{\sum_T h_{T,E}}{\sum_T M_T\, \hat{Z}_T\, e^{-E/k_{\text{B}}T}}, \tag{4.11}$$

$$\hat{Z}_T = \sum_E \hat{g}_E\, e^{-E/k_{\text{B}}T}. \tag{4.12}$$

This intermediate result is used to calculate a new estimate for the partition function. For simulations with 128 temperature threads up to 10^5 successive iterations of (4.11) and (4.12)

were used to refine both estimates and reach convergence. Since both quantities assume typically very large values their logarithms are implemented instead to avoid floating point overflow. Recall that the logarithm of the density of states provides an estimate for the entropy (2.14). To obtain the density of states and the entropy as a continuous function of energy, Bezier smoothing [50] was used. Finally, advanced analysis techniques such as microcanonical inflection-point analysis [42] can be applied to the entropy curve and its higher derivatives, which provides additional indicators to locate structural phase transitions.

4.4 Implementation

In order to develop a fast C++ program it was most effective to begin the implementation in a straightforward manner while "bottlenecks" were identified by measuring the cpu-time in a second step.

Computationally most demanding is the evaluation of the system energy $E(\mathbf{X})$. The expression for the acceptance rate (4.5) exemplifies that even for simple displacement updates the change in energy is required to determine whether the update is accepted. Therefore, an efficient evaluation of the energy (3.6) is vital.

The expression on the right hand-side of (3.6) was separated to avoid the recalculation of parts which are unaffected by a given Monte Carlo update. For instance, after a displacement update, only interactions that involve the moved monomer will change. The energy due to the contact of the i^{th} monomer with the substrate $E_{\text{S},i} = U_{\text{S,c}}(\vec{r}_i)$, c.f. (3.7), was stored in an array. Since energies of different monomers i are independent, the sum of all surface contacts was stored in a separate variable $E_{\text{S}}(t)$. Once a surface energy changed only in the i^{th} monomer the previous contribution was subtracted and the new contribution was added,

$$E_{\text{S}}(t+1) = E_{\text{S}}(t) - E_{\text{S},i} + \sum_{a=1}^{\infty} U_{\text{S}}(r_{ia}). \tag{4.13}$$

Recall that index a labels vertices of the substrate, c.f. (3.6). A similar approach was chosen for the bonded and non-bonded potentials. However, since these potentials are pair potentials, all pairs must be stored. To avoid the comparison of monomer indices and the calculation of memory positions, a constant two-dimensional array of pointers was used to store the memory address of a pair interaction for all possible combinations of monomer indices. Besides this efficient utilization of memory, another performance gain was achieved by exploiting symmetries of the system under consideration.

The calculation of the interaction of a monomer $\vec{r}_i$ with the surface requires the distance to all surface sites within Lennard-Jones cutoff distance r_c. In order to avoid high memory demand only 10 substrate vertices were stored. In Fig. 4.2 the substrate is shown with its triangular Wigner-Seitz cells. The idea behind this algorithmic approach utilizes that symmetry transformations applied to the lattice do not change the set of distances between vertices and the monomer located at $\vec{r}_i$. In turn, these operations can be applied to a copy of the monomer $\vec{r}_i{}'$ leaving distances to lattice vertices invariant. Here, $\vec{r}_i{}'$ is shifted by lattice vectors towards the origin. Two further copies $\vec{r}_i{}''$ and $\vec{r}_i{}'''$ are generated by rotation of $2\pi/3$ about the origin, see Fig 4.2. In this way only vertices between the lattice vectors $\vec{v}_1$ and $\vec{v}_2$ and within Lennard-Jones cutoff distance need to be considered. The cutoff is shown as a dashed curve in Fig. 4.2 b).

For each copy of the monomer the surface interaction is evaluated in groups of increasing monomer-vertex distance, see Fig 4.2, starting with $\{\vec{s}_1, \vec{s}_2\}$ (gray) and followed by $\{\vec{s}_3, ..., \vec{s}_5\}$ (orange) and $\{\vec{s}_6, ..., \vec{s}_{10}\}$ (brown). Once all distances between a monomer copy (which is generally located above the surface plane) and the vertices in one set is larger than the Lennard-Jones cutoff radius, the evaluation of subsequent sets can be omitted for this copy.

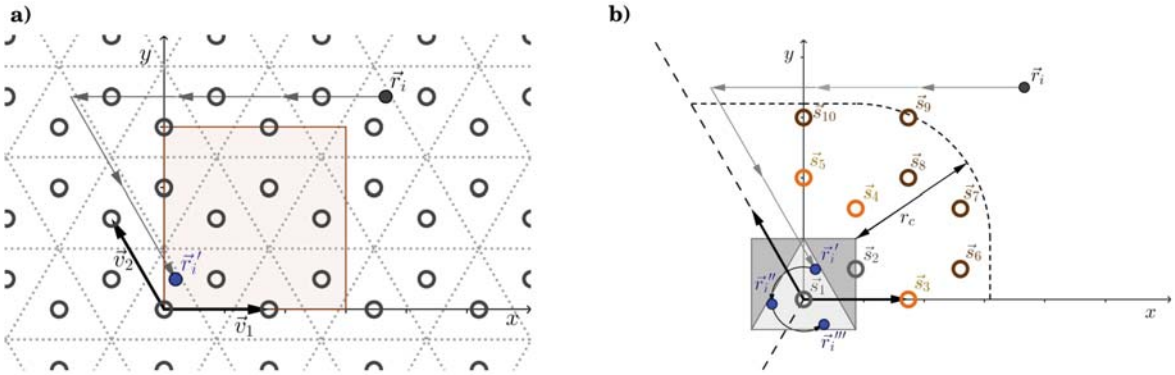

Figure 4.2: a) Vertices of the hexagonal substrate are illustrated by circles, Wigner-Seitz cells are indicated by dotted lines. In order to determine all distances between monomers and surface vertices, the monomer $\vec{r}_i$ is translated by integer multiples of the lattice vectors $\vec{v}_1, \vec{v}_2$ towards the fundamental cell. b) The new monomer position $\vec{r}_i{}'$ is located in the Wigner Seitz cells close to the origin, marked in gray. The dashed curve indicates the area which is within Lennard-Jones cutoff distance r_c to the gray shaded rectangle. Two additional copies of the monomer, $\vec{r}_i{}''$ and $\vec{r}_i{}'''$, are created by applying $2\pi/3$ lattice rotations about the z-axis, so that only lattice vertices $\vec{s}_1, ..., \vec{s}_{10}$, located in the sector between the two lattice vectors, are required. After Liewehr and Bachmann [15].

4.5 Pseudo-random number generation

The random numbers in this simulation were generated with the pseudo-random number generator developed by Marsaglia and Zaman [48]. This is a lagged-Fibonacci generator combined with a generator based on an arithmetic sequence for a prime modulus. The quality is checked by examining the autocorrelation time and applying with a uniformity and parking lot test [49]. Finally, the random number generator in combination with the used algorithm was tested for small system sizes against existing results.

Chapter 5

Adsorption behavior of homopolymers on hexagonal surfaces

In this chapter the adsorption behavior of a homopolymer on a hexagonal substrate is examined. As in previous studies [13, 43, 44] the polymer is grafted onto a fixed surface. Here, a hexagonally patterned substrate i.e. a honeycomb lattice is chosen, mimicking the structure of a graphene sheet. The results presented in the following reveal the response behavior of the polymer at different temperatures and adsorption strengths of the surface. Results of a small system with $N = 13$ monomers are presented first in order to outline the general arrangement of typical structural phases which are known from previous polymer adsorption studies. First effects of the substrate pattern are found by comparison with the flat continuous surface. Since the complexity of encountered structural phases increases with the system size, a detailed discussion of subphases, in the low temperature regime is provided subsequently for the 55mer. Subphases show qualitative, structural similarities and are separated by phase specific order parameters. The system sizes were chosen to allow for a comparison of ground state structures, discussed in Section 5.2.1. Finally, with the description of low temperature phases at hand, the physics of the pattern recognition process is investigated.

5.1 Adsorption of short polymer chains N = 13

The smallest system that was studied is the homopolymer chain consisting of N = 13 monomers. In order to outline the particular effects of pattern recognition upon the surface adsorption the results are compared to the case of a continuous surface [16].

5.1.1 Transition signals in the specific-heat curves

The starting point for the discussion of the adsorption behavior on a hexagonal surface is the specific-heat curve for the 13mer, which is obtained as a continuous function from the reweighted density of states. In Fig. 5.1 the specific heat is shown for increasing values of the surface adsorption strength $0.0 < \varepsilon_S < 4.0$.

For $\varepsilon_S = 0.0$ specific-heat curves are shown for different values of the asymmetry parameter η in the bonded potential, which was defined in eq. (3.3). The differences of specific-heat curves in a) are larger then the statistical error. In panel a) the error bars, omitted for clarity, are of the same size as shown in b). A pronounced peak of finite width at about $T = 0.3$ indicates the location of the freezing transition which is due to the finite size not restricted to a single point. At higher temperatures the Θ-transition, where globule liquid-like conformations expand into random coil gas-like conformations, is signaled by a "shoulder" in the specific heat. All subsequent simulations were curried out with $\eta = 0.1$.

Increasing the adsorption strength to $\varepsilon_S = 0.2$ reduces the height of the peak, see Fig. 5.1 b). The unimodal shape of the canonical histograms of the different temperature threads, shown in Fig. 5.2, classifies both signals as second- or higher-order transitions. In order to determine the effect of the substrate on the structural transition, the shape of the specific-heat curve is examined by plotting canonical averages for the intramolecular and monomer-substrate interactions separately. Due to the small value of the surface adsorption strength the overall behavior is governed by interactions within the polymer and is thus

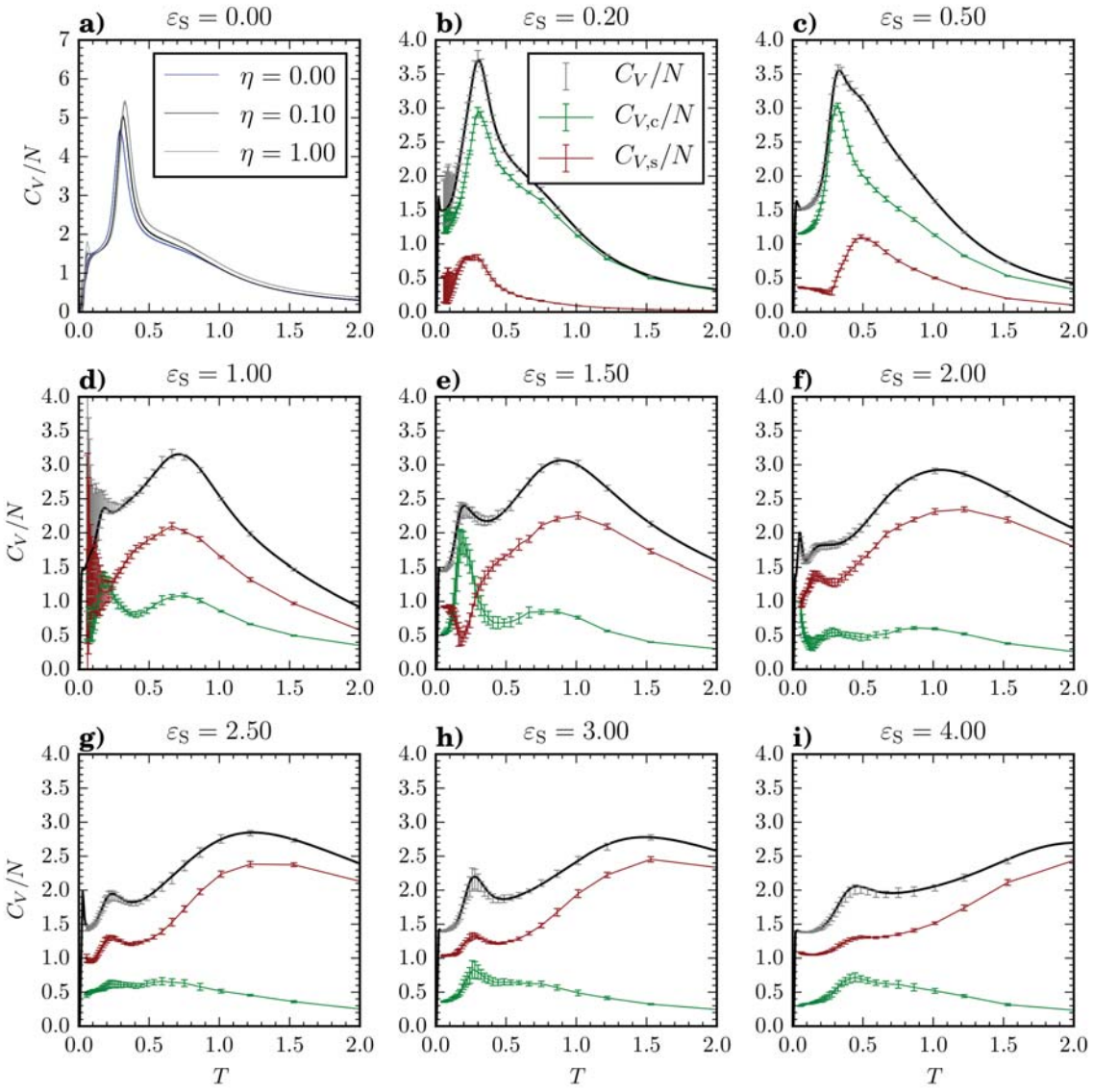

Figure 5.1: The specific heat $C_V(T)/N$ of a 13mer is presented for different surface adsorptions strengths $0.0 < \varepsilon_S < 4.0$. In panel a) the specific-heat curves obtained from multiple histogram reweighting is shown for different values of the control parameter η (c.f. Fig. 3.2), where the interaction with the surface is turned off, $\varepsilon_S = 0.00$. Error bars are of the size as shown in b). Panel b)-i) shows reweighted specific-heat curves for increasing adsorption strengths where $\eta = 0.1$ (black, solid curve). Canonical averages of the total specific heat (gray), contributions from interactions within the polymer chain $C_{V,c}$ (green) and from monomer-surface interactions $C_{V,s}$ (red) obtained from 40 temperature threads are depicted as data points with error bars.

similar to the case of a free polymer. This behavior is retained if the adsorption strength is increased to a value of $\varepsilon_S = 0.5$, however, it can be noted that the stronger attraction to the surface leads to an increase in temperature of the signal in the surface contribution. Examining the geometrical structure of conformations at this temperature reveals that this signal can be associated with the wetting of the polymer on the surface.

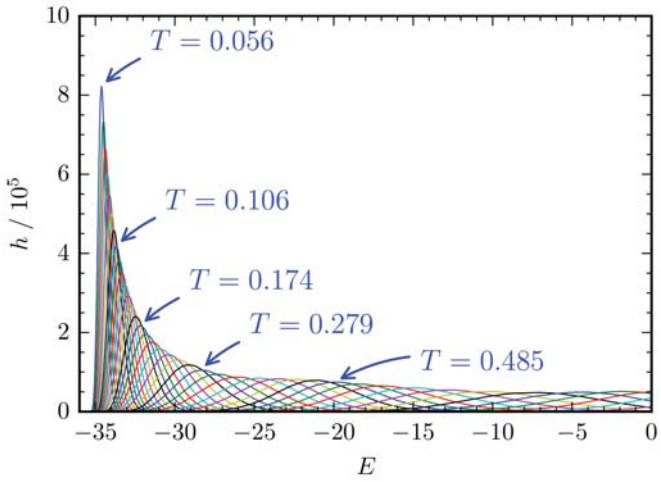

Figure 5.2: The canonical histograms of a 13mer with $\varepsilon_S = 0.20$ is shown for 40 temperatures $T = 0.06, ..., 6.15$ which are proportional to the canonical energy distribution, eq. (2.13). Temperatures of blue curves are given on the figure. All histograms show a unimodal shape, so that structural transitions are classified as higher-order transitions. Large overlap of the histograms allows for high acceptance rates of parallel-tempering replica-exchanges.

This first insight into the type of the physical process is used to determine additional order-parameters that can signal the transition of interest. The generic choice for the Θ-transition, where gas-like expanded random-coil conformations collapse into liquid-like globule conformations, is the fluctuation of the squared radius of gyration

$$r_{\mathrm{gyr}}^2 = \frac{1}{N}\sum_{i=1}^{N}(\vec{r}_{\mathrm{com}} - \vec{r}_i)^2 \qquad \text{with} \qquad \vec{r}_{\mathrm{com}} = \frac{1}{N}\sum_{i=1}^{N}\vec{r}_i. \tag{5.1}$$

Applying the fluctuation dissipation theorem (2.16) to the measured mean value of squared radius of gyration yields

$$\frac{\mathrm{d}\langle r_{\mathrm{gyr}}^2\rangle}{\mathrm{d}T} = \frac{\langle r_{\mathrm{gyr}}^2\, E\rangle - \langle r_{\mathrm{gyr}}^2\rangle\, \langle E\rangle}{k_{\mathrm{B}}T^2}. \tag{5.2}$$

However, since this quantity describes the compactness, it is expected to show only a weak signal for a wetting transition from a desorbed globule into a adsorbed globule phase. It is thus beneficial to consider only the z-component of the radius of gyration perpendicular to the surface $r_{\mathrm{gyr},z}$, the z-component of the center of mass z_{com} or the number of monomers $n_{S,z_{\mathrm{lim}}}$ below a threshold z_{lim}. The threshold value is chosen according to the expected geometrical differences of the structure.

These three additional structural order parameters facilitate the discrimination of different subphases. However, the comparably small number of the degrees of freedom of a 13mer limit the number of expected subphases. A direct classification by visual inspection was found to be most efficient for this small system. A detailed discussion of additional order parameters will be provided for larger system sizes which allow for more subtle arrangements of subphases.

Returning to the specific heat in Fig. 5.1 d)-i) as the major quantity, a further increase of the surface adsorption strength leads to a dominant influence of the monomer surface interaction on the structure formation process. As a result of the additional surface interactions the collapse transition becomes more pronounced for $\varepsilon_{\mathrm{S}} \geq 1.0$ than the freezing transition.

5.1.2 Structural hyperphase diagram

With the fluctuations of the different energetic contributions at hand, transitions between phases can be located. Graphing the transition signals with respect to temperature and the generic surface adsorption strength parameter ε_{S} leads to a structural hyperphase diagram.

At high temperatures typical polymer conformations are stretched out at a large distance from the surface which defines the desorbed expanded phase (DE), see top row in Fig 5.3. If the attraction towards the surface is increased, adsorption sets in at higher temperatures, which explains the positive slope of the transition band. The thickness of the transition band is a finite-size effect and accounts for the fact that different order parameters indicate different transition temperatures. The phase of adsorbed expanded conformations (AE) is located below the adsorption transition band, which crosses at $\varepsilon_{\mathrm{S}} = 1.2$ the collapse transition separating expanded from globule phases. The mean value of the energy changes gradually between the desorbed expanded (DE) and desorbed globule (DG) so that instead of the weak "shoulder" in the specific heat, Fig. 5.1, the radius of gyration was used to extend the collapse transition band towards low surface adsorption strengths. Curves of the radius of gyration are discussed in more detail for the 55mer in Section 5.2.

For temperatures $T < 1.0$ the structure formation of the polymer is affected by the hexagonal surface pattern. Energetically favorable positions for monomers are located in the centers of hexagonal rings. Intramolecular interactions prevent monomers from reaching these attractive sites in the surface plane for adsorption strengths $\varepsilon_S < 1.5$ so that the desorbed globule phases (DG) is found. This phase is separated from the adsorbed globule phase by the wetting transition which extends the adsorption transition into the low temperature regime and finally merges with the freezing transition at $\varepsilon_S = 0.2, T = 0.3$. Note that collapse and freezing transition are only weakly dependent on the surface adsorption strength. Below the freezing transition, in the adsorbed compact phase of conformations with 3 and 2 layers, the location of monomers is more ordered than in the liquid like globule phases. Since surface interactions dominate for $\varepsilon_S > 0.8$, the pattern recognition is enhanced.

In this study, the lattice constant and the equilibrium bond length r_0 were chosen to be equal. Due to the finite character of the FENE bond, two adjacent monomers cannot occupy neighboring attractive centers of the honeycomb structure. At least one more monomer in

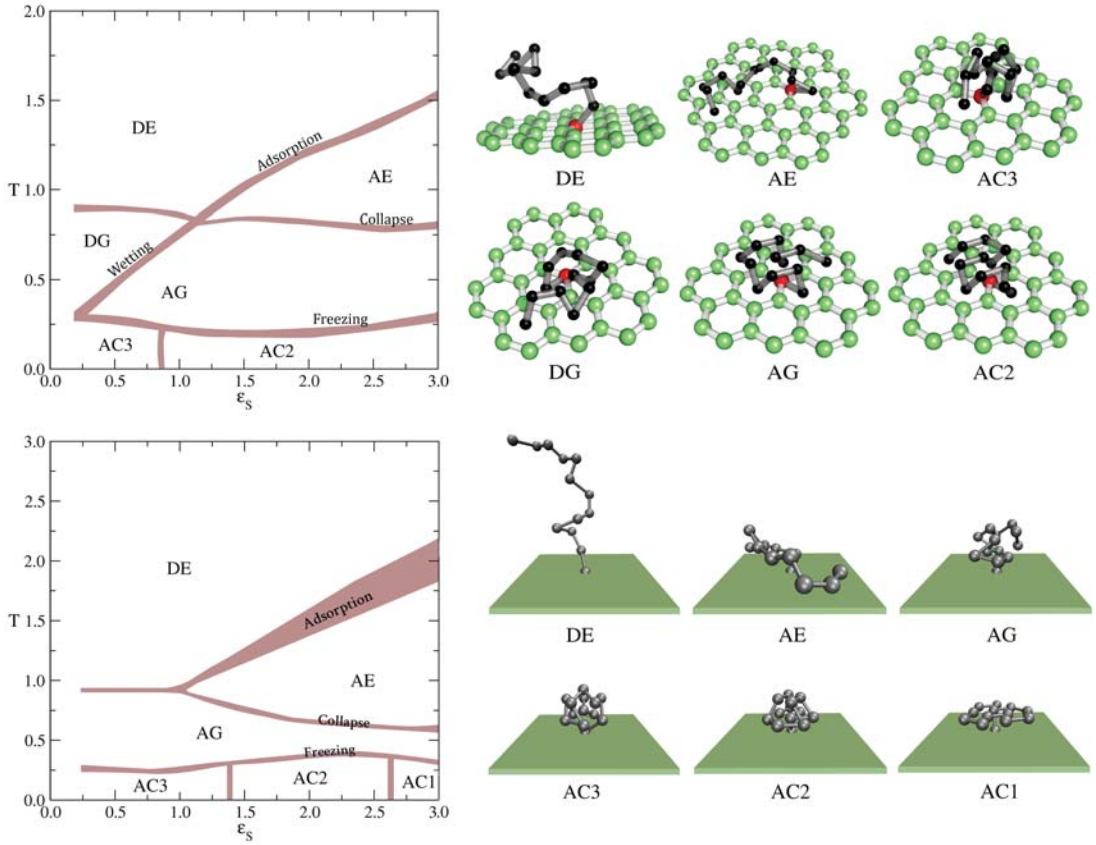

Figure 5.3: The structural hyperphase diagrams of the grafted 13mer on a hexagonal surface and a flat continuous surface [16] parametrized by adsorption strength ε_S and temperature T are presented aside with representative conformations of the discovered phases. For the adsorption on a hexagonal surface the structural phases are classified into desorbed expanded (DE), desorbed globule (DG), adsorbed expanded (AE), adsorbed globule (AG), adsorbed compact with double layer (AC2), and adsorbed compact with triple layer (AC3). For comparison the phases of the flat continuous case are indicated analogously. An important difference is the missing desorbed globule (DG) phase and therefore the missing wetting transition. In addition, an adsorbed compact mono layer (AC1) is found for low temperatures and high adsorption strengths.

between is required, and it resides above the surface and can form a bridge between monomers at these most favorable lattice sites. Therefore, a adsorbed compact monolayer (AC1) which is observed for the flat continuous surface does not occur on a hexagonal lattice.

The comparison of the hyperphase diagrams of the hexagonal substrate and the continuous flat surface (see Fig. 5.3, lower row) reveals a second effect of the patterned surface: the existence of the desorbed globule phase. For the flat surface even very small ε_S values cause adsorption of globular conformations. Monomers can adsorb to any location on the surface without creating a competition with intramolecular interactions. In the patterned case the number of accessible adsorption centers is limited, leading to a much stronger entropic suppression of adsorbed conformations. Moreover, adsorption to the pattern imposes constraints on the remaining monomers inside the globule structure. Therefore, the minimal adsorption strength required for adsorption to the patterned substrate increases with temperature, resulting in a similar slope for the wetting transition as it was observed for the adsorption transition of expanded structures.

5.2 Outline of the adsorption behavior of a 55mer

As in the case of a 13mer, starting point of the canonical analysis of the homopolymer with $N = 55$ constituents is the specific heat as function of temperature. Shifts and separations of transition signals are discernible in Fig. 5.4 where the specific heat is plotted for 50 values of the surface adsorption strength $\varepsilon_{\mathrm{S}} \in [0.0, 5.0]$. In panel a) transition signals are found for $T < 0.6$. Comparably large heights in the peaks of the specific heat are observed for small values $0.0 < \varepsilon_{\mathrm{S}} < 0.2$ and intermediate adsorption strengths $1.05 < \varepsilon_{\mathrm{S}} < 1.50$. Strong transition signals are typically associated with phase transitions from disordered to ordered phases, exhibiting internal symmetry, which are discussed in section 5.3 in the context of a structural analysis.

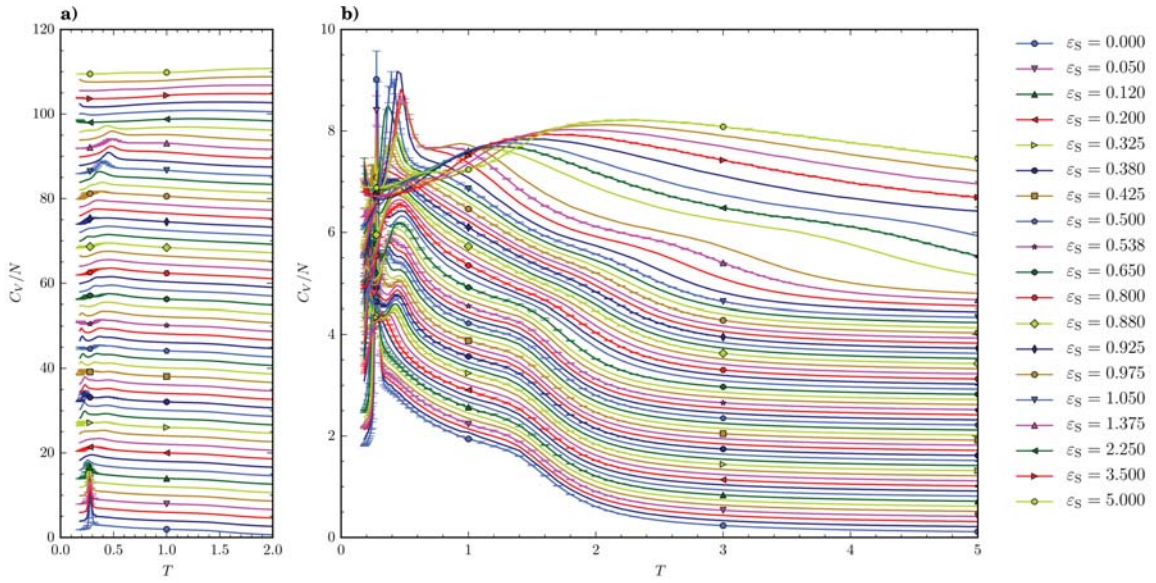

Figure 5.4: The specific heat is presented as a function of temperature $C_V(T)$ of a 55mer for 50 different surface adsorptions strengths $\varepsilon_S \in [0.0, 5.0]$. Panel a) shows the low temperature behavior, curves for subsequent ε_S are shifted vertical by $\Delta C_V = 50$. For high temperatures the same curves are shown with a vertical shift of $\Delta C_V = 5$ in b).

The same specific-heat curves are presented on a different scale in Fig. 5.4 b) where the "shoulder" caused by the Θ-transition becomes apparent. For low adsorption strengths the Θ-transition is found at $T = 1.6$ and shifts towards higher temperatures for $\varepsilon_S > 0.8$. Note, that the spacing of simulated adsorption strength is not uniform but adjusted to the location of phases.

In Fig. 5.5 the structural hyperphase diagram of a 55mer is presented for the physically relevant parameter space in temperature T and surface adsorption strength ε_S. Starting point for the discussion of the adsorption behavior is the well studied limiting case of very small monomer-substrate interactions.

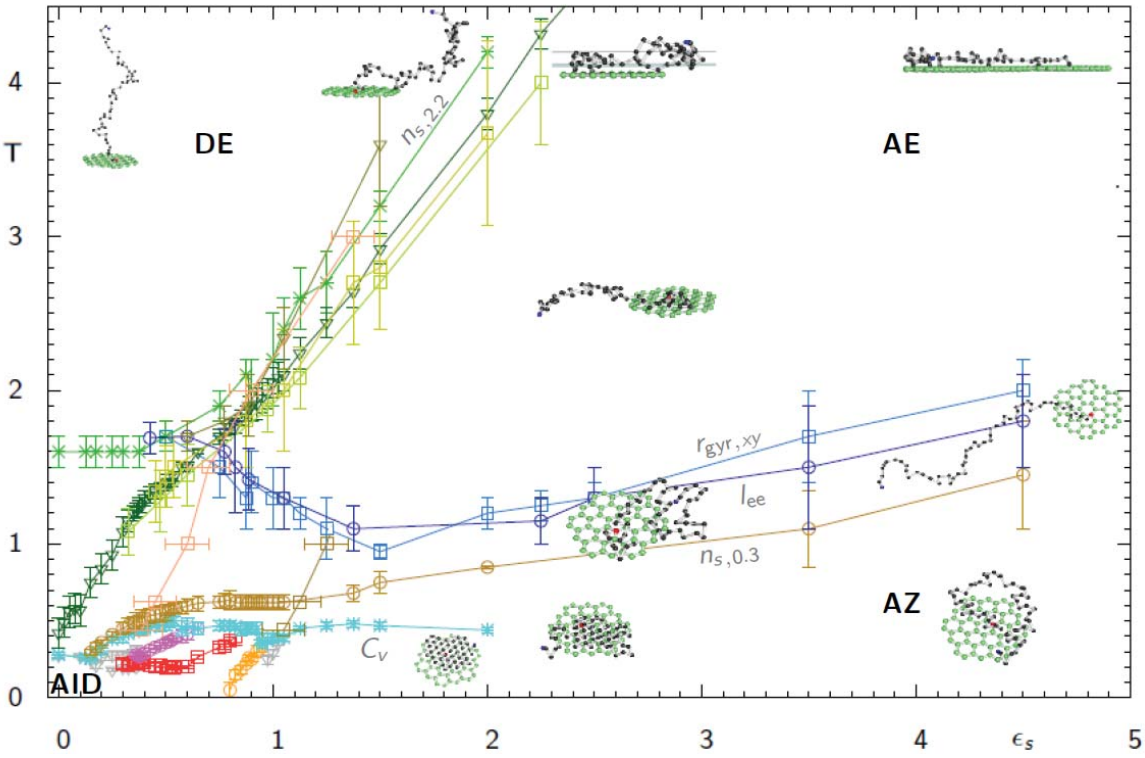

Figure 5.5: The structural hyperphase diagram of a 55mer grafted on a hexagonal surface is parametrized by the temperature T and surface adsorption strength ε_S. The limiting phases at low and high temperatures are the adsorbed icosahedral droplet (AID) phase and the desorbed expanded (DE) phase at small surface adsorption. The adsorbed *zig-zag* (AZ) and adsorbed expanded phase (AE) are found for high ε_S values.

5.2.1 Adsorbed icosahedral droplet phase (AID)

For low temperatures and vanishing adsorption strength the system is in a frozen phase. Typical for a flexible, elastic homopolymer with 55 constituents is a crystal structure with icosahedral shape. The core of the structure can be identified with the icosahedron observed for the 13mer while the remaining 42 monomers form a complete overlayer, embracing the core of the structure.

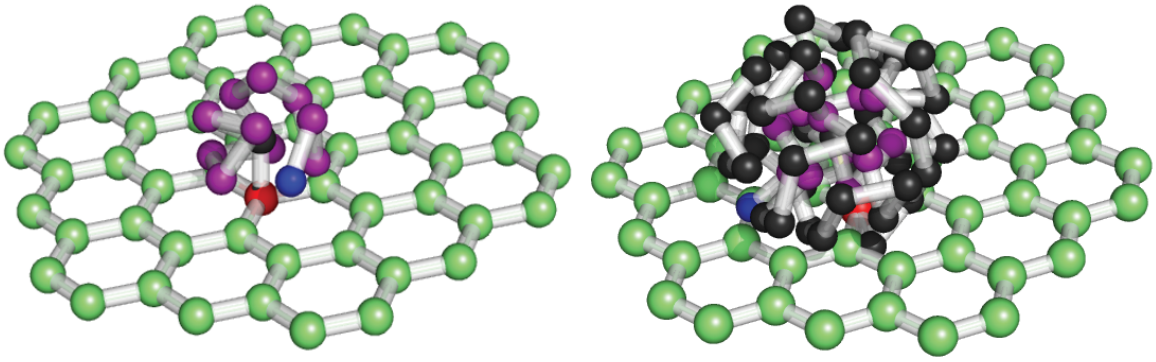

Figure 5.6: An icosahedron is well known as the ground state conformation of a 13mer and observed for $\varepsilon_S = 0$ (left). For vanishing surface interaction the 55mer forms the same core structure with 13 monomers indicated by purple while the remaining 42 monomers form a complete overlayer on the core structure (right). The grafted and the open end of the polymer chain is colored in red and blue, respectively.

Since monomer-monomer distances within spherical layers differ from the distance between layers, this structure requires a flexible character of the bonds and is, for example, not observed for a bead stick model [13]. In Fig. 5.6 icosahedral structures for system sizes $N = \{13, 55\}$ at $\varepsilon_S = 0$ are depicted, where the monomers are constrained to reside in the positive half space above the surface. Monomers in the outer shells are observed very close to vertices of the surface. This is especially the case for the 55mer since the surface curvature, compared to the 13mer, is reduced while the grafted monomer imposes the contact of polymer with the substrate surface. Once the interaction with the surface is turned on, the repulsive character of the Lennard-Jones interaction between lattice vertices and monomers in the shell breaks the icosahedral symmetry. Due to the divergent behavior of the Lennard-Jones potential for small distances, this effect can be observed for non-zero adsorption strengths and becomes dominant for $\varepsilon_S > 0.18$. For smaller adsorption strengths the adsorbed icosahedral droplet phase (AID) is found. The next larger system size that allows for a complete overlayer on the icosahedral conformation is $N = 147$.

5.2.2 Polymer behavior for small adsorption strengths

Increasing the temperature at $\varepsilon_S < 0.18$, the crystal starts to desorb and to melt. Although globular shapes initially persist, structural symmetries inside the molecule break up, which is indicated by a peak in the specific heat. Dewetting from adsorbed globule into desorbed globule phase is associated with the number of monomers that are in energetic contact with the surface. Recall that the Lennard-Jones cutoff, which formally limits the height of the surface interaction, was introduced to simplify the calculation. It was chosen at a distance where the potential has sufficiently decayed (3.1). Hence, the cutoff height $r_c = 5\sigma/2$ should not be of any physical significance but serves as an upper bound for the distance of essential surface interaction.

The attractive force to the surface becomes maximal at $r_{F,\max} = \sqrt[6]{\frac{13}{7}}\, r_0 \approx 1.11$. A lower bound for the distance where surface attraction becomes negligible can therefore be given by the location of the inflection point of the force magnitude $r_{F,\text{infl}} = \sqrt[6]{\frac{13\cdot 14}{7\cdot 8}}\, r_0 \approx 1.22$. Consequently the numbers of surface contacts $n_{s,1.5}$ and $n_{s,2.2}$ provide clear signals for the adsorption transition. The separation of the liquid-like (DG) and gas-like phase (DE) is prominently signaled by the fluctuations in the z-component of the radius of gyration. Finally, the polymer enters the gas phase where the structure is unfolded into desorbed expanded (DE) conformations.

5.2.3 Effect of increasing adsorption strength on low-temperature behavior of the polymer

Starting from the origin of the phase diagram Fig. 5.5 more interesting and model parameter specific features are found when the surface interaction is turned on. Already for small surface interactions the symmetry of the icosahedral ground state is broken. Increasing the surface parameter ε_S, a landscape of transition lines is found separating structural phases which

recognize the pattern of the substrate, see Fig. 5.5. The spherical structure starts to flatten out, leading to a variety of structures where the lowest layer of monomers recognizes the pattern of the hexagonal surface. One order parameter that allows one to distinguish phases with pattern recognition from disordered phases, is the number of surface contacts, defined by the number of monomers below a certain threshold value of the Cartesian z-component, perpendicular to the surface. For the chosen surface potential, the particular threshold value of $z = 0.3$ counts the number of monomers occupying favorable lattice sites, located in the center of the hexagons of the substrate. At temperatures above the pattern-recognition transition, the polymer still remains absorbed. However, polymers closest to the surface float in a perpendicular distance between $1.0 < z < 2.2$ allowing the structure to move (mostly unconstrained) parallel to the surface. Details and subphases in this regime will be presented in a more detailed scope in Section 5.3.

At $\varepsilon_{\mathrm{S}} = 1.0$ the properties of polymer beads and surface beads coincide, leading for low temperatures to compact film-like structures. Increasing the absorption strength further conformations expand on the surface in order to maximize the number of polymer beads in the centers of the hexagons. The interactions between non-bonded monomers become less important. For very high surface adsorption strengths low temperature conformations are structurally more similar to those dominating the adsorbed expanded phase, which is typically associated with random structures.

5.2.4 Collapse of adsorbed phases: expansion on the surface

Increasing the temperature at high adsorption strengths leads initially to an expansion of the conformations parallel to the xy-surface plane. This two-dimensional expansion is signaled by the radius of gyration in the xy-direction, see Fig. 5.7. Starting from low temperatures the surface parallel radius of gyration $\langle r_{\mathrm{gyr},xy} \rangle$ increases and for high epsilon values exhibits a peak in the temperature interval $T \in [1.6, 3.6]$. Inflection points mark the maximum of

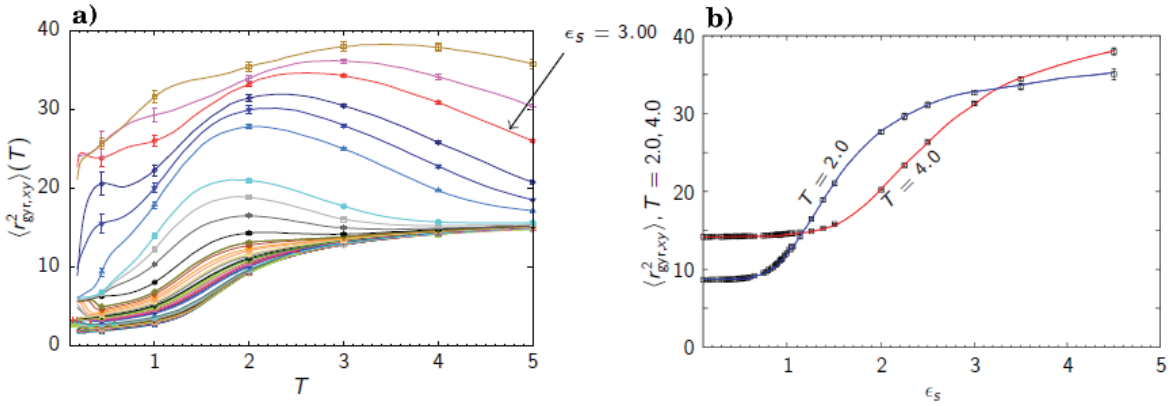

Figure 5.7: The surface parallel, squared radius of gyration $\langle r^2_{\mathrm{gyr},xy} \rangle$ illustrates the expansion of the polymer on the substrate, here shown as a function of temperature for various adsorption strengths $0.0 < \varepsilon_{\mathrm{S}} < 4.5$ a) and as function of adsorption strength b). Structural phase transitions are associated with points of highest absolute slope.

thermal fluctuations, indicating a phase transition, see Fig. 5.7 a). At higher temperatures it seems at first glance counter-intuitive that the xy-component of the radius of gyration decreases. However, the radius of gyration in the z-direction shows that the still adsorbed conformations start to extend into the third dimension. This effect is denoted as a topological transition.

5.2.5 Desorption: surface perpendicular expansion

For dominant surface adsorption strengths $\varepsilon_{\mathrm{S}} \geq 2.0$ the radius of gyration in the surface perpendicular direction is negligibly small for temperatures $T < 2$, see Fig. 5.8 a), indicating that the polymer is fully adsorbed. The comparison with the component of the radius of gyration parallel to the surface, Fig. 5.8 b), reveals that both quantities are anticorrelated: Once the desorption from the surface sets in, the two-dimensional expansion is reduced.

At $\varepsilon_{\mathrm{S}} = 2.0$ this anticorrelated behavior starts at $T = 2.0$, for stronger surface attraction the desorption process shifts to higher temperatures. To quantify this observation

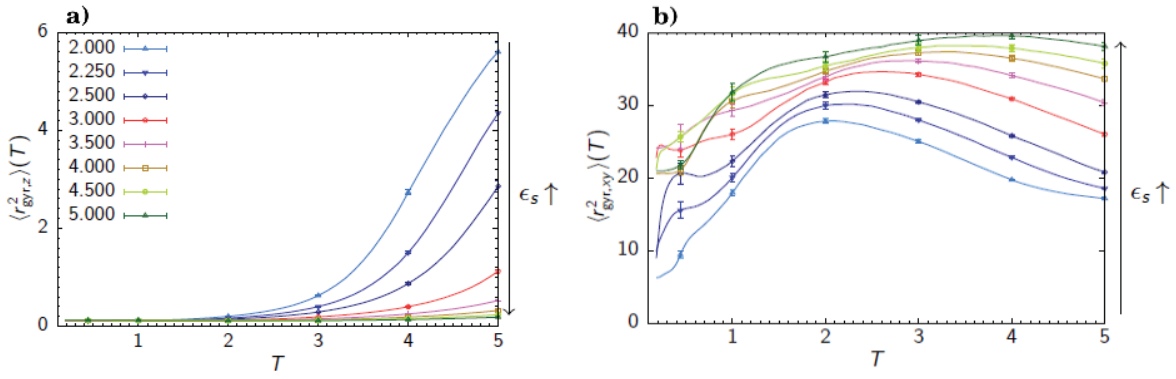

Figure 5.8: Surface perpendicular and surface parallel, squared radius of gyration are compared as functions of temperature for $2.0 < \varepsilon_S < 5.0$.

the derivative of thermodynamic and structural quantities with respect to the adsorption strength parameter is necessary. In Fig. 5.7 b) the radius of gyration in xy-direction is shown for constant temperatures as a function of ε_S. Inflection points in these plots confirm the location of the adsorption transition band in Fig. 5.5.

5.3 Phases, subphases and pattern recognition of a 55mer

Focusing on the region of temperatures $T < 2.0$ and $\varepsilon_S < 1.5$ a landscape of subphases can be found in the regime of the adsorbed compact phases where pattern recognition has set in, see Fig. 5.9. The specific heat was used primarily to identify transitions for low temperatures $T < 0.5$. Note, that merging signals and steep transition bands require a detailed scan of the parameter space with independent parallel tempering simulations. In this study it was necessary to vary the control parameter by about $\Delta\varepsilon_s \approx 0.025$ where transition lines were expected. Next, structural quantities were used to make more quantitative distinctions. Due to technical constraints of the parallel tempering method, the lowest temperature was

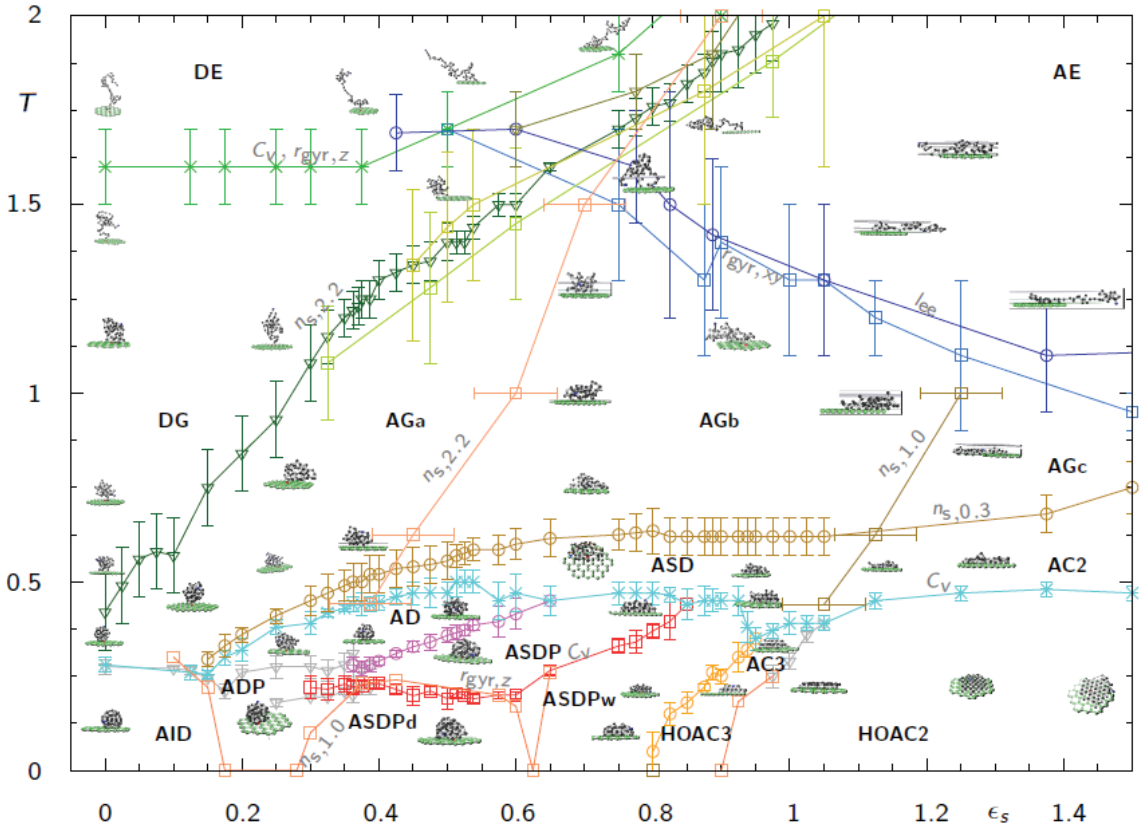

Figure 5.9: The detailed $T - \varepsilon_S$ hyperphase diagram displays the structure of a vast landscape of subphases on the regime of frozen-like structures below $T < 0.5$ and adsorbed globule structures (AG) below $T < 1.5$. Transitions between frozen-like structures obtained from signals in the specific heat. For the extrapolation of vertical transition lines (orange) characteristics in the form of the number of monomers $n_{s,1.0}$ where used as described in section 5.3.1. The freezing transition (turquois) is accompanied by a transition, associated with a large fluctuation in the number of occupied hexagonal centers $n_{S,0.3}$ (brown). At temperatures $T > 0.5$ the wetting transition and transitions between adsorbed globule subphases are signaled by the number of surface contacts $n_{S,2.2}$ and $n_{S,1.0}$ respectively. The collapse transition for adsorbed structures shows pronounced signals in the surface parallel component of the radius of gyration and in the end-to-end distance of the polymer (light blue, dark blue). The collapse transition between desorbed phases is signaled by "shoulders" in the specific heat and located by peaks in the surface perpendicular component of the radius of gyration (green). Error bars on transition bands indicate the width of peaks in response quantities, resulting from finite-size effects.

generally chosen as $T = 0.18$. Sufficient sampling at lower temperatures was only possible with the use of increased computational effort and was, therefore, only performed for a few temperatures.

5.3.1 Extrapolation of vertical transition lines in the low-temperature region

At very low temperatures $T < 0.2$ thermal fluctuations become small and conformations in the same phase resemble an unique ground state morphology. Consequently, curves of structural quantities as functions of temperature bend and converge towards a limiting value, see Fig. 5.10. An order parameter is suitable if it exhibits different values for neighboring phases. Therefore, the fluctuations in the order parameter become comparably large at a transition bands. For instance, the z-component of the center of mass as well as the number

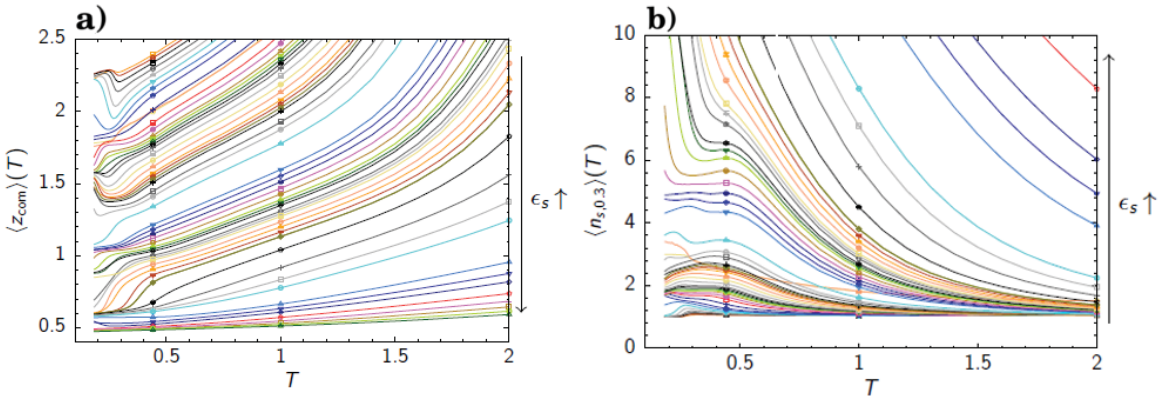

Figure 5.10: a) Mean values of the z-component of the center of mass z_{com} are presented for $\varepsilon_{\text{S}} \in [0.0, 5.0]$ which bend for low temperatures to unique limiting values . For increasing values of ε_S the adsorption to the surface is enhanced so that the value of the center of mass generally decreases. b) Similar grouping is observed for the number of occupied adsorption centers $n_{S,0.3}$. The crossing line in this set of curves indicates insufficient sampling and results from this simulation are disregarded.

of occupied adsorption centers in the substrate $n_{S,0.3}$ allow for a clear discrimination of phases. The thickness of the transition bands become smaller with decreasing temperature.

In the adsorption strength interval from $0.0 < \varepsilon_S < 1.5$ six subphases are found at the lowest simulated temperatures (Fig. 5.10), which are illustrated in the magnified view of the complete hyperphase diagram Fig. 5.9. Starting from small adsorption strengths, these are the adsorbed icosahedral droplet (AID) and adsorbed droplet phase with pattern recognition (ADP), followed by the dewetted and wetted semispherical subphases (ASDPd) and (ASDPw), respectively, before highly oriented phases in three and two layers are found (HOAC3, HOAC2).

5.3.2 Adsorbed droplet phases AID, ADP, AD

The detailed discussion of the adsorbed icosahedral droplet phase in Section 5.2.1 was provided as the starting point of the general outline of the considered phase diagram. The perfect icosahedron is formed for $\varepsilon_S = 0$. However, a less symmetric conformational phase, with shifts in the minority of polymer beads, persists for $\varepsilon_S < 0.18$.

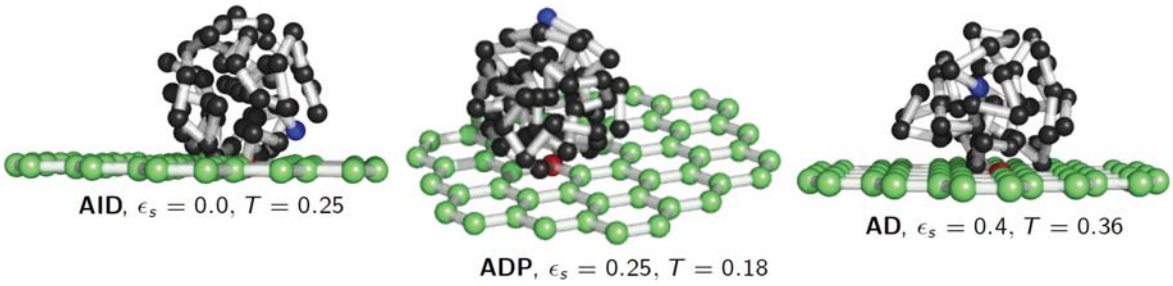

Figure 5.11: A typical conformation for the adsorbed icosahedral phase (AID), found for $\varepsilon_S < 0.18$, is shown (left) together with two adsorbed droplet conformations (ADP, AD), where the former structure is a representative of the patterned subphase ADP.

For higher adsorption strengths, monomers facing the hexagonal surface recognize the pattern. Increased values for the number of surface contacts $n_{S,0.3}$ document the occupation of centers in the hexagonal ring structure of the substrate, see Fig. 5.10 a). Although an overall spherical shape is still retained, the influence of the pattern reduces the internal symmetry, forming the ADP phase. Towards higher temperatures, the ADP phase is separated by signals in $r_{\mathrm{gyr},xy}$ from the adsorbed droplet (AD) phase where thermal fluctuations average out the discrete character of the pattern. Occasionally, monomers at the curved surface deform the spherical shape, but the attractive character of the substrate facilitates the formation of relatively dense droplets. This interplay of the entropy-driven thermal and energy-driven adsorption effects can be perceived by the non-zero slope of transition bands in the phase diagram Fig. 5.9, blue and purple lines. These bands obtained from specific heat signals show an extension of the AD phase towards higher adsorption strengths if the temperature is increased.

5.3.3 Adsorbed semispherical phases ASDPd, ASDPw, ASDP, ASD

Towards higher ε_S values droplets are attracted more strongly by the surface and exhibit a semispherical shape. At low temperatures the ADP phase is followed by the dewetted and wetted semispherical droplet phases (ASDPd) and (ASDPw) which are distinguished by their height and patterned surface contacts, resembling the properties of adhesive or cohesive liquid-surface interactions. However, since in this coarse-grained study specific properties of materials are generalized, the semispherical droplet with highest surface coverage is denoted more generically as a wetted conformation, see Fig. 5.12 top row. At temperatures $T > 0.2$ the ASDP and the ASPDw phases are observed.

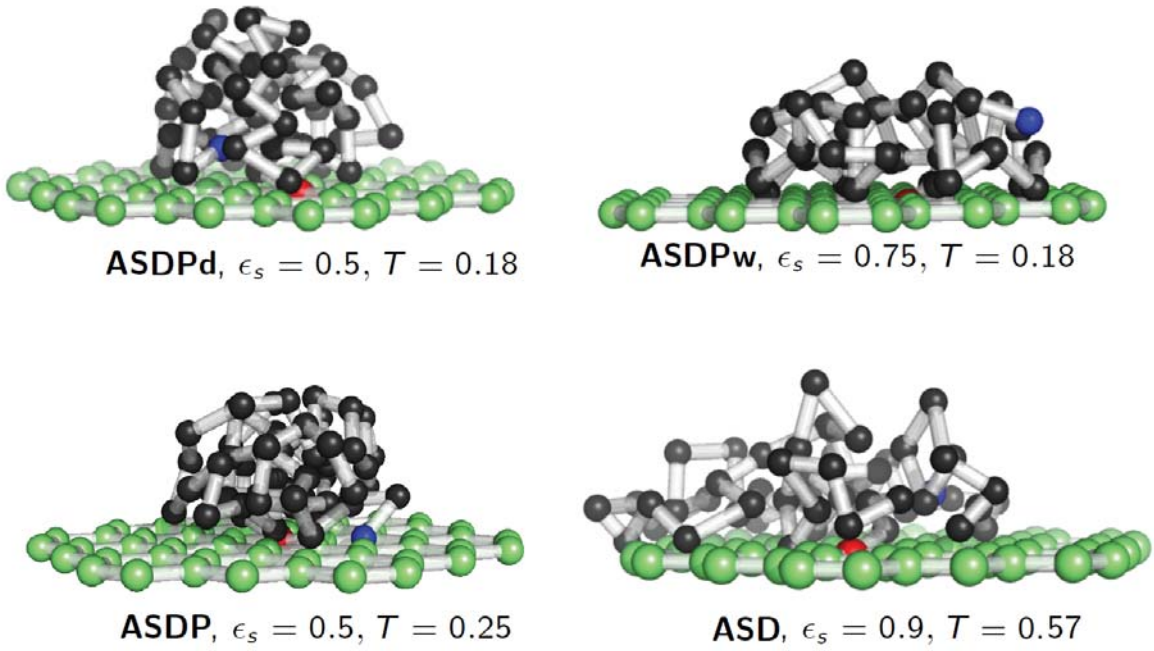

Figure 5.12: For low temperatures adsorbed semispherical droplets which recognize the pattern are classified into dewetted and wetted subphases (ASDPd) and (ASDPw), shown in the upper row. Fluctuations increase at higher temperatures in the ASDP phase while all centers in the covered surface are occupied. At $T > 0.45$ the semispherical droplets are adsorbed to the surface and occupy hexagonal centers at irregular locations (ASD), shown in the bottom right.

As a precursor of the freezing transition the specific heat signals form a horizontal transition band, Fig. 5.9 (blue line at $T = 0.45$), which separates phases that are dominated by the pattern and surface effects from amorphous structures that float with an semispherical shape above the surface (ASD). Although single contacts to the hexagonal centers are established, monomers in the surface layer of ASD conformations are in the minority. Vacant hexagonal centers underneath the polymer structure can be observed as a result, see Fig 5.12. Fluctuations in $n_{S,0.3}$ separate this phase from globule subphases, Fig. 5.9 (golden line at $T \approx 0.6$). For $\varepsilon_S < 0.55$ bands deduced from C_V and $n_{\mathrm{S},0.3}$ merge into a single freezing transition band. The latter is well known from the free polymer case.

5.3.4 Adsorbed compact triple layers HOAC3, AC3

For very specific values of the absorption strength $0.8 < \varepsilon_S < 1.0$ a highly oriented adsorbed compact phase of conformations with three layers (HOAC3) is found, see Fig. 5.13. This terminology is derived from highly oriented pyrolytic graphite (HOPG). A HOPG crystal is one instance for a suitable substrate material that exhibits a hexagonal surface.

Due to its morphology, the HOAC3 phase describes a technologically relevant polymer phase, which is a candidate for surface coatings in various applications and can possibly be used for mechanical stabilization of two dimensional materials such as graphene.

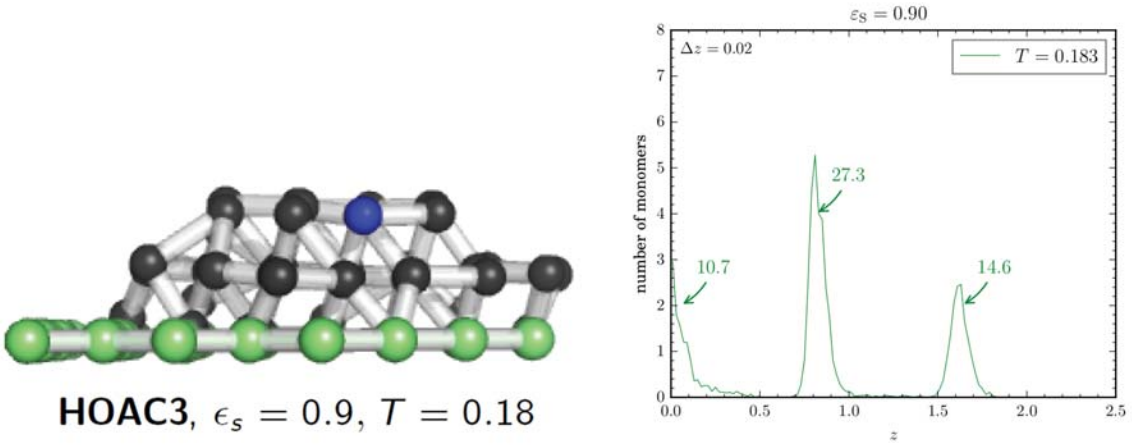

Figure 5.13: In the highly oriented adsorbed compact triple layer phase (HOAC3) monomers in the surface layer complete the hexagonal substrate pattern to an triangular lattice. Two triangular overlayers arrange in a face-centered cubic (fcc) or hexagonally close packed (hcp) configuration. Heights of the separate layers are identified in the normalized histogram n_z (right) as $z = \{0.01, 0.81, 1.62\}$. The average number of monomers in each layer is indicated on the peaks.

The lowest layer of polymer beads in the HOAC3 phase occupies all vacant centers of honeycomb substrate in the covered area and completes the hexagonal lattice to a triangular lattice. The remaining monomers arrange in triangular overlayers. Usually about 15 of the 55 monomers form a small third layer which covers a single part of the larger second layer in a compact manner without leaving vacancies. All three layers can be found as distinct

peaks in the histogram of the height in Fig. 5.13 (right). The size of the bins is $\Delta z = 0.02$. Numbers indicate how many monomers are contained in each peak. Note that the number of monomers in the second layer is approximately three times higher than in the first layer, since in the first layer 2 vertices per triangular cell are provided by the substrate. This property becomes important to distinguish phases at higher values of ε_{S} and will be discussed in the subsequent Section 5.3.5. The histogram also confirms that differences in the earlier defined number of surface contacts $n_{S,0.3}, n_{S,1.0}, n_{S,1.5}, n_{S,2.2}$ can be used to determine the number of monomers in each layer and also between layers. The latter case, that monomers reside between layers is expected for higher temperatures.

In this structural phase three highly oriented layers form either a face-centered cubic (fcc) or a hexagonally close packed (hcp) lattice type, see Fig. 5.14. A small energetic difference exists due to different distances between a monomer in the third layer and an interaction site in the surface layer. Where an ABC stacking of triangular lattices is found in fcc lattices, hcp lattices are formed by AB stacking. The smallest distances are summarized, together with resulting potential energies, in Table 5.1. Since the vertices of the hexagonal substrate provide lattice points in the surface layer, the energetic contribution depends on the adsorption strength. In the parameter interval $0.9 < \varepsilon_{\mathrm{S}} < 1.0$, relevant for HOAC2, the fcc structure shows the highest energy, see Fig. 5.14. For the hcp lattice the energy per monomer in the third layer differs for $\varepsilon_S \neq 1$, depending on whether it is located directly above a substrate vertex (hcp1) or a polymer bead (hcp2). Both cases occur with a ratio of 1:2, leading to an overall energy difference between fcc and hcp of about $\Delta E \approx 0.3$, where approximately $n_3 = n_{S,2.2} - n_{S,1.0} \approx 14.6$ monomers in the third layer were considered. Since the Boltzmann constant is set to unity this value is associated with the temperature where differences in the occurrence of lattice types become significant. However, it should be noted that this energy margin is directly proportional to the system size.

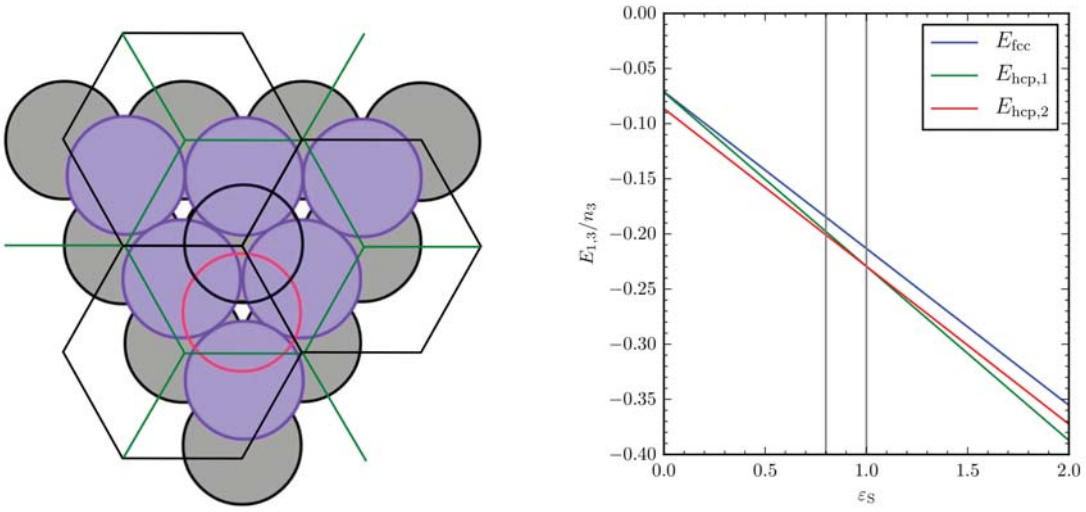

Figure 5.14: The first and second triangular layer is represented by filled circles in gray and violet, respectively. For face centered cubic packing (fcc) monomers in the third layer are located on top of two holes (red circle), creating ABC stacking. For this lattice type, lattice points in different layers align when viewed under an angle $\phi = \tan^{-1}(\sqrt{2}) \approx 54.7°$. Hexagonally closed packing (hcp) is observed when monomers in the third layer are located on top of monomers in the first layer (black circle), creating AB stacking. At adsorption strengths $\varepsilon_S \neq 1$ two cases can be distinguished. In one case a monomer is located directly above a substrate vertex (black hexagons), denoted as hcp1, where in the case of hcp2 it is placed above a polymer bead (green hexagons). The energy, due to interactions between monomers in the first layer and a single monomer in the third layer $E_{1,3}/n_3$, is given for each type of packing as a function of the surface adsorption strength (right).

Table 5.1: Next nearest neighbor distances between monomers in the first and third layer are given together with energies per monomer for the hcp (left) and the fcc configuration (right).

i	count	r_i/r_0	$U_{LJ}(r_i)/10^{-3}$
1	1	$\frac{\sqrt{24}}{3} \approx 1.632$	-86.37
2	6	$\frac{\sqrt{33}}{3} \approx 1.915$	-23.84
3	6	$\frac{\sqrt{51}}{3} \approx 2.381$	0

i	count	r_i/r_0	$U_{LJ}(r_i)/10^{-3}$
1	3	$\sqrt{3} \approx 1.732$	-56.39
2	3	$\sqrt{4} \approx 2.000$	-14.69
3	6	$\sqrt{5} \approx 2.236$	0

A prevalence of hcp structures at low temperatures should therefore become measurable for larger system sizes. Generally this crystal-like phase is observed where the adsorption strength is large enough that the substrate pattern can impose long range ordering effects, but is still small enough that the formation of additional layers is attractive. For adsorption strengths close to $\varepsilon_S = 1$, crystal growth in the direction perpendicular to the surface occurs generally only on overlayers which are larger than the Lennard-Jones radius. The growth of an overlayer along an existing edge on a large surface where the number of attractive contacts is maximized is energetically preferred. Finally, it explains why the HOAC3 phase is found for adsorption strengths less than unity.

The limiting factor for the number of overlayers is the length of the polymer chain. For longer polymers the formation of 4 layer crystal phase is expected close to the left transition line of the HOAC3 phase in Fig. 5.9. However, even for this small system size we recognize that the growth into the surface perpendicular direction leads to a pyramidal shape of the polymer. Since monomers in the third layer avoid locations close to the edge of the second layer slanted faces are formed, similar to a truncated polygonal pyramid. This can be seen in Fig. 5.13 on the left end of the structure. Therefore, we conclude, that long-range ordering causes significant changes in the overall shape of the polymer compared to the adjacent semispherical phase ASDPw.

For temperatures $T > 0.3$ thermal fluctuations smear out the internal symmetry which defines the AC3 phase. Partitioning of the third layer into a fcc and a hcp regions accompanied by defects and vacancies at the interface can occur. This effect is expected to become statistically relevant for larger system sizes.

The properties of the HOAC3 and AC3 phase, discussed here, are specific to the lattice constants of the substrate and locations of potential minima of the bonded and non-bonded interaction. In this study all three parameters were chosen to be equal, allowing for the formation of crystal structures without defects. We conjecture, that increasing the differences

between these parameters creates frustration effects in large conformations and narrows the adsorption strength interval, where layered polymer phases are observed.

Phases similar to HOAC3 and AC3 are expected for other substrate patterns, e.g. for a square lattice, however, less energetic contacts than in the studied case of a hexagonal substrate will reduce the stability of the phase, so that long-range ordering, i.e. ordering on the length scale of the entire polymer, is already lost at lower temperatures.

5.3.5 Adsorbed compact double layers HOAC2, AC2

Increasing the adsorption strength causes the crystal-like structures to flatten into double layer conformations. Bonds between the first and second layer are required to connect beads in the favorable lattice sites in the center of the hexagons as it was observed for the previously discussed HOAC3 phase. For a large parameter interval $0.9 < \varepsilon_{\mathrm{S}} < 2.0$ conformations are compact and cover a circular area on the surface, which is denoted as the highly oriented adsorbed compact phase in two layers (HOAC2). Note that for a triangular double layer a distinction into a fcc or a hcp lattice is obsolete.

Three types of bonds are observed in the HOAC2 phase: Type 1, bonds parallel to the surface in the triangular overlayer. Type 2, steep bonds that connect monomers in the centers of the hexagons with the overlayer and type 3, bonds less steep on the fringe of the film-like structure where two monomers in the surface layer are connected by one monomer in the second layer. In Fig. 5.15 this *zig-zag* shaped type 3 is marked in purple. To determine the relevance of fringe effects, the ratio of monomers in different layers is used.

$$R = \frac{n_{S,1.5} - n_{S,0.3}}{n_{S,0.3}} \tag{5.3}$$

Considering the surface layer only, one substrate vertex contributes to the 3 surrounding hexagons. Thus, the 6 vertices in hexagonal cell contribute with one third each, resulting in

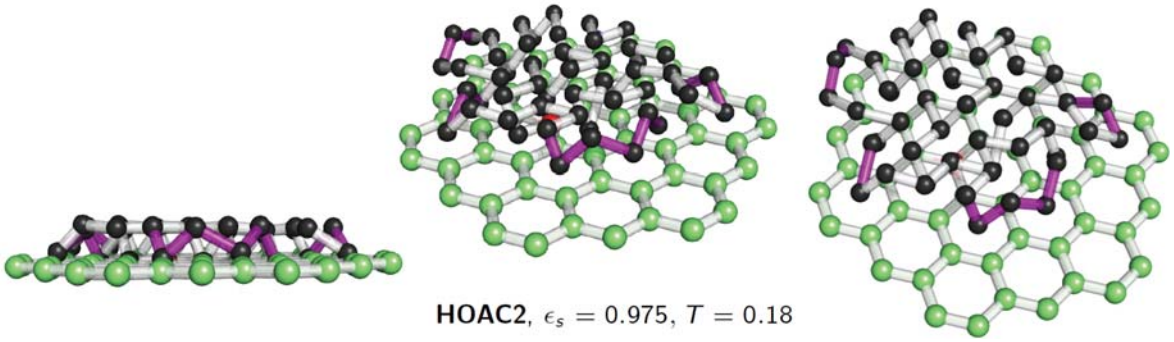

Figure 5.15: One representative conformation of the highly oriented adsorbed compact double layer phase (HOAC2) is shown from three different perspectives. The uniform height of the overlayer is observed from the side view (left). In the centered panel surface parallel bonds and bonds which connect monomers in the centers of the hexagons (surface layer) with the second layer become visible. Surface monomers in the center of the conformation are connected by two or more beads, located in the second layer. On the edge of the structure surface monomers are connected by one monomer in the second layer forming *zig-zag* shaped bonds indicated with purple color. On the right the conformation is viewed under a 54.7° angle, displaying the remarkable alignment of both triangular lattices.

2 effective vertices per cell. One polymer bead is now placed in the center of the hexagonal cell so that a triangular lattice is formed. In the triangular overlayer all 3 effective monomers in a hexagonal cell are provided by the polymer.

Therefore, we conclude that in systems much larger than the 55mer where the fringe of the film like structure can be neglected the ratio between polymer beads in the surface layer and monomers in the upper layer is $R = 1/3$. In this case three surface parallel bonds (type 1) are, on average, followed by two steep bonds that connect into the centers of hexagons (type 2).

With fringe effects taken into account the ratio will increase towards the limiting ratio of about $R = 1$ if the system size is reduced to very small systems. This maximum ratio is also observed for the 55mer at very high values the adsorption strength $\varepsilon_S > 2$, where the polymer

maximizes the number of monomers inside the hexagons. The associated adsorbed zig-zag phase (AZ) is discussed in the subsequent section. The analysis of the surface to overlayer ratio R can also be applied to the two or more layered crystals and even for semi-spherical patterned droplets, since the surface layer is formed in the same way once the hexagonal pattern is recognized.

5.3.6 Adsorbed *zig-zag* phase AZ and quenching

Monomer-surface interactions become dominant if $\varepsilon_S > 2$. The number of monomers inside the hexagonal substrate cells is maximized. The restricted length of the FENE bond allows the occupation of attractive centers by every second monomer in the chosen parametrization. The third monomer is centered above a substrate bond between the two monomers located in the surface and forms in perpendicular direction a bridge for both adjacent monomers. The polymer bonds in this adsorbed phase exhibit a *zig-zag* shape, defining the AZ phase.

The location of the central monomer is constrained by the repulsive character of the surface potential. It cannot be so close to the surface that all energetic demands can be satisfied at once. Instead, the repulsion between the bridging monomer and nearby substrate vertices requires either that bonds are stretched or that monomers inside the attractive rings are slightly lifted off from the substrate plane.

The grafted end of the polymer chain can possess an abnormally steep bond to a monomer in the second layer, since the first monomer is chosen as one surface vertex. Grafting in the center of a hexagon would cure this minor defect. For the cases shown in Fig. 5.16 the grafted monomer, depicted in red, exhibits a surface parallel bond, connecting a second monomer which is located in the center of a hexagon.

On the left-hand side of Fig. 5.16, the complete chain reveals bonds in zig-zag configuration. Even at the lowest simulated temperature this structure shows a dilute coverage of the substrate. On smaller scales a frequent change in the direction of *zig-zag* bonds is

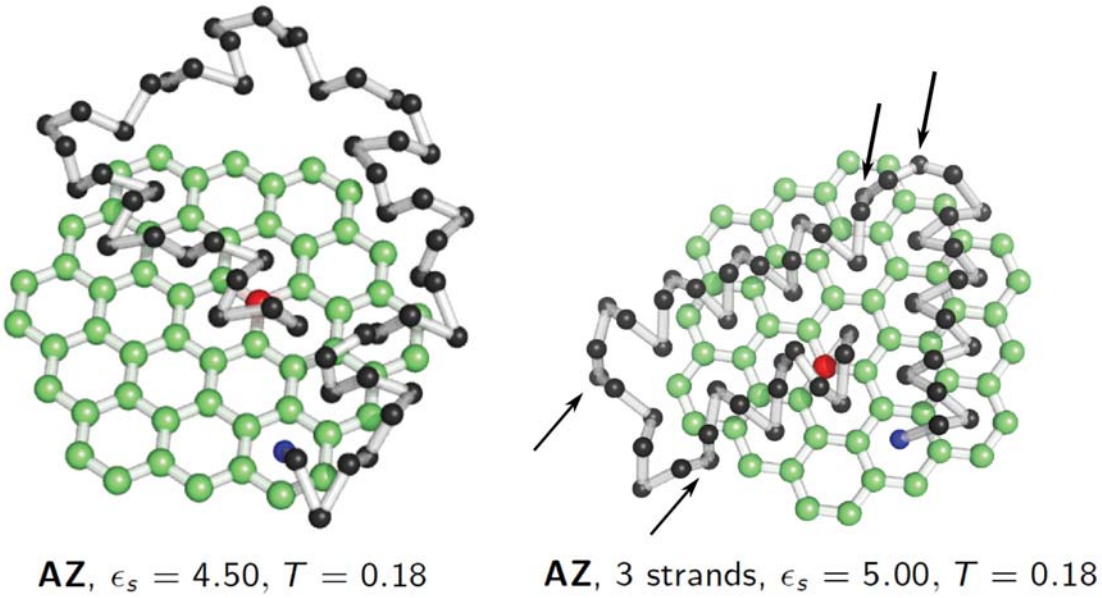

Figure 5.16: At high surface adsoption strengths the polymer maximizes the occupation of hexagonal centers, which leads to a *zig-zag* arrangement of bonds. Even for the lowest sampled temperatures, the polymer covers the surface in an irregular manner, leading to vacancies in the center of the structure (left). This effect of poor sampling due to strong energetic barriers was attacked with additional rotational pivot updates. With this improved Monte Carlo update the interplay of local and global ordering effects was observed, leading to the formation of three straight strands which fold into a compact tertiary structure. Kinks at the end of each strand are marked by arrows.

observed which establishes additional short-range monomer-monomer interaction. Parallel tempering with simple displacement updates was not able to reveal more compact, entropically suppressed structures during the typical simulation time of 10^9 Monte Carlo updates per site (Monte Carlo sweeps). The reason are strong energetic barriers between different pathways of *zig-zag* conformations on the substrate. As solution to this problem more advanced algorithms like Wang-Landau simulations [49] or multicanonical sampling [50] could be employed. In this case the implementation of an additional Monte Carlo update turned out to be most efficient.

Inspired by the short-range ordering effects in AZ configurations, we proposed a rotational pivot update about monomers residing at the attractive centers. In order to naturally increase the acceptance rate, the rotational angle was constrained to the discrete rotational symmetries of the lattice.

A conformation from this improved simulation is shown in Fig. 5.16 (right). For a low energy configuration it is now found that the direction of the *zig-zag* bridge alters in a regular manner allowing the polymer to occupy centers of hexagons in two parallel rows. Within this straight secondary structure, denoted as a strand, monomers establish non-bonded interactions with multiple adjacent *zig-zag* bridges which leads to local ordering.

An additional global ordering effect breaks the symmetry of the structure on a larger length scale, allowing *zig-zag* strands to fold into a tertiary structure of closely packed strands. In the conformation presented in Fig. 5.16 (left) non-bonded interactions between different strands are established and overcompensate energetically disadvantageous arrangements of zig-zag bridges in the end of strands, where two connected strands exhibit kinks, indicated by arrows.

The structural shape and the interplay of local and global ordering effects, observed here, are closely related to the behavior of semi-flexible polymer with torsion potential. In [30] the formation of helical structures and their adsorption to a surface was investigated. There, the torsional potential led to a local ordering effect causing arrangement into helices. However for specific parameter values these structures folded into helix bundles which were adsorbed to the surface, allowing for geometrically similar structures as observed here in the AZ phase.

5.3.7 Relevance of ground states behind high energetic barriers

Monte Carlo simulations aim generally at the sampling of the entire configuration space to satisfy ergodicity in order to describe thermodynamic properties in equilibrium. If the results of the simulation are compared to an experiment, it is important to verify that the

experimental setup allows for the same ergodic behavior. Strong barriers in the system that are circumvented in a simulation by sophisticated updates may cause quenching effects in an experiment. A fast decrease in temperature, for example, would lead to quenching of disordered structures into the frozen phase as it is observed for glasses. Conditions that allow for proper thermal equilibrium cannot be deduced directly from Monte Carlo simulations since under thermal conditions monomers do not follow smooth trajectories but rather perform a random walk in state space. However, the demand of advanced updates hints at the question, under which conditions conformations like the folded *zig-zag* strand become physically relevant. Further simulations based on molecular dynamics are suggested to resolve this interesting problem.

5.3.8 General properties of solid-like phases

From the detailed analysis of separate phases the following general conclusions can be made for solid-like phases. By increasing the system size from a 13mer to a 55mer a dramatic increase of distinguishable phases was observed. Especially in the regime of frozen phases $T < 0.5$ a diversity of subphases was encountered where internal polymer interactions compete with monomer-substrate interaction, $0.1 < \varepsilon_S < 1.1$. We conclude that cooperative effects and long-range ordering requires a minimum number of system constituents. Since one end of the homopolymer was grafted to the surface, all configurations at low temperatures reside closely to the surface. For polymers which are not grafted it is expected that conformations at low temperatures exhibit a more pronounced desorption transition. These characteristic properties are summarized in a simplified schematic phase diagram, see Fig 5.17. For different adsorbed phases, such as the HOAC3 or the ASD phase, it was conjectured that an increase in system size, or a change in the size and shape of the surface pattern, reveals new interesting behavior.

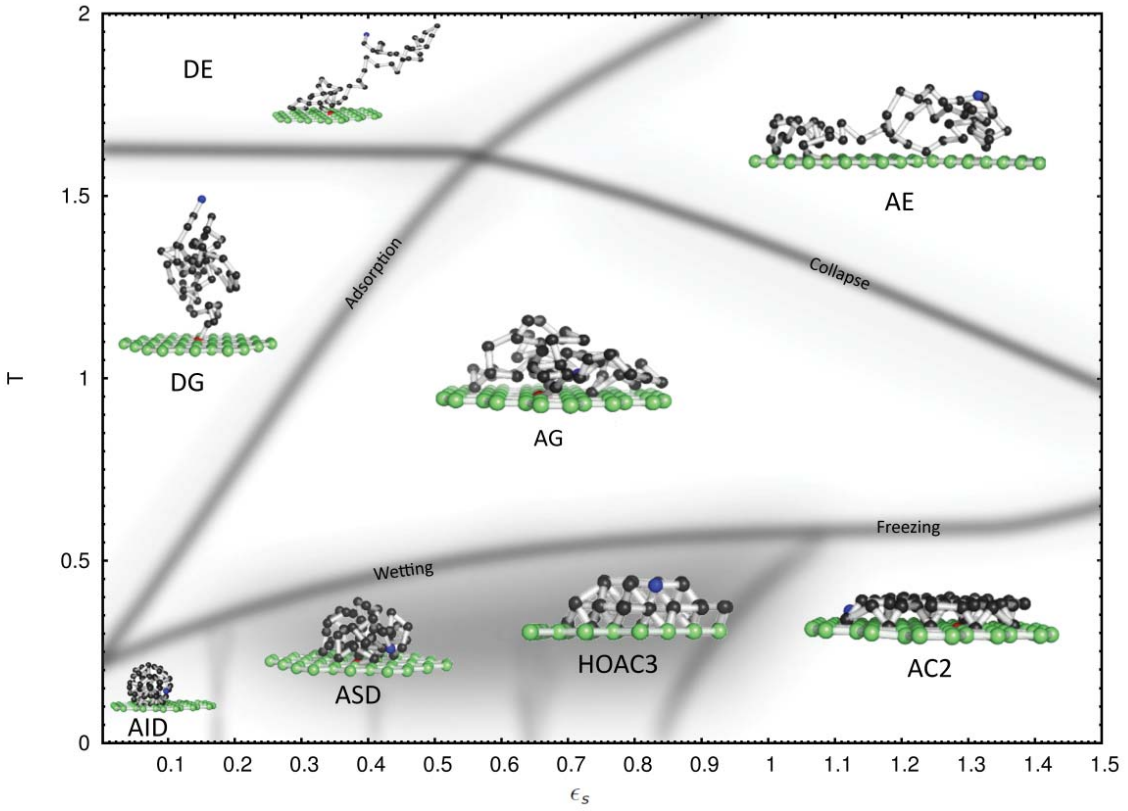

Figure 5.17: This simplified version of the structural hyper phase diagram [15], exemplifies by means of representative conformations the major differences of solid-, liquid- and gas-like polymer phases, separated by wetting and freezing, as well as adsorption and collapse transitions. Gray transition bands indicate the non-zero width of structural phase transitions due to the finite size of the system. Solid subphases in the low temperature regime, presented in Fig 5.9 are indicated by gray color.

5.3.9 Liquid-like globule phases DG, AGa, AGb, AGc

The morphology of the desorbed globule phase (DG) is similar to the discussed case of shorter chains in section 5.1. Globule phases are located between $0.5 < T < 1.6$ and $0.0 < \varepsilon_S < 0.5$, see Fig. 5.9. Passing the adsorption transition, signaled by fluctuations in the number of surface contacts $n_{S,2.2}$, the polymer is affected by the attractive surface. Compared to solid-like droplet structures the density of conformations in the adsorbed globule phase

AG is reduced. Monomers inside the globule move freely, while the center of mass is only constrained by the grafted end of the polymer chain. The majority of monomers resides at heights $z > 1.0$ where the pattern of the combined surface potential is already smeared out, see Fig. 3.3 c) and d).

5.4 Recognition of the hexagonal pattern

The analysis of the structural hyperphase diagram revealed two distinct ways how a homopolymer can recognize the hexagonal pattern. In this section triangular overlayering is compared to the formation of zig-zag bonds.

5.4.1 Analysis of the height distribution

From the analysis of the subphase regime we found that the HOAC3 phase exhibits most prominently ordering effect which are imposed on the polymer by the substrate. The HOAC3 phase shows together with AC3, HOAC2 and AC2 triangular symmetries where surrounding phases in the phase diagram such as AZ, ASD, ASDPw exhibit a different alignment to the substrate pattern. In order to investigate the origin of the observed pattern effects, we examine now the distribution of the monomer height z in the different phases which can quantify pattern recognition. In Fig. 5.18 a)-f) the histogram of the height of monomers is presented for increasing adsorption strengths $\varepsilon_S = \{0.00, 0.50, 0.90, 1.00, 2.50, 4.50\}$ at four different temperatures in each panel. Every histogram was obtained from 100 uncorrelated structures where the bin size of each histogram is chosen as $\Delta z = 0.02$. Numbers at selected peaks indicate the number of monomers found at the peak location. Starting point of the discussion are the signals for the HOAC3 phase in plot Fig. 5.18 c) at $T = 0.18$, which is also shown in Fig. 5.13. Histograms collected at higher temperatures reveal properties of distinguished phases. According to the phase diagram, Fig. 5.9, the parameters

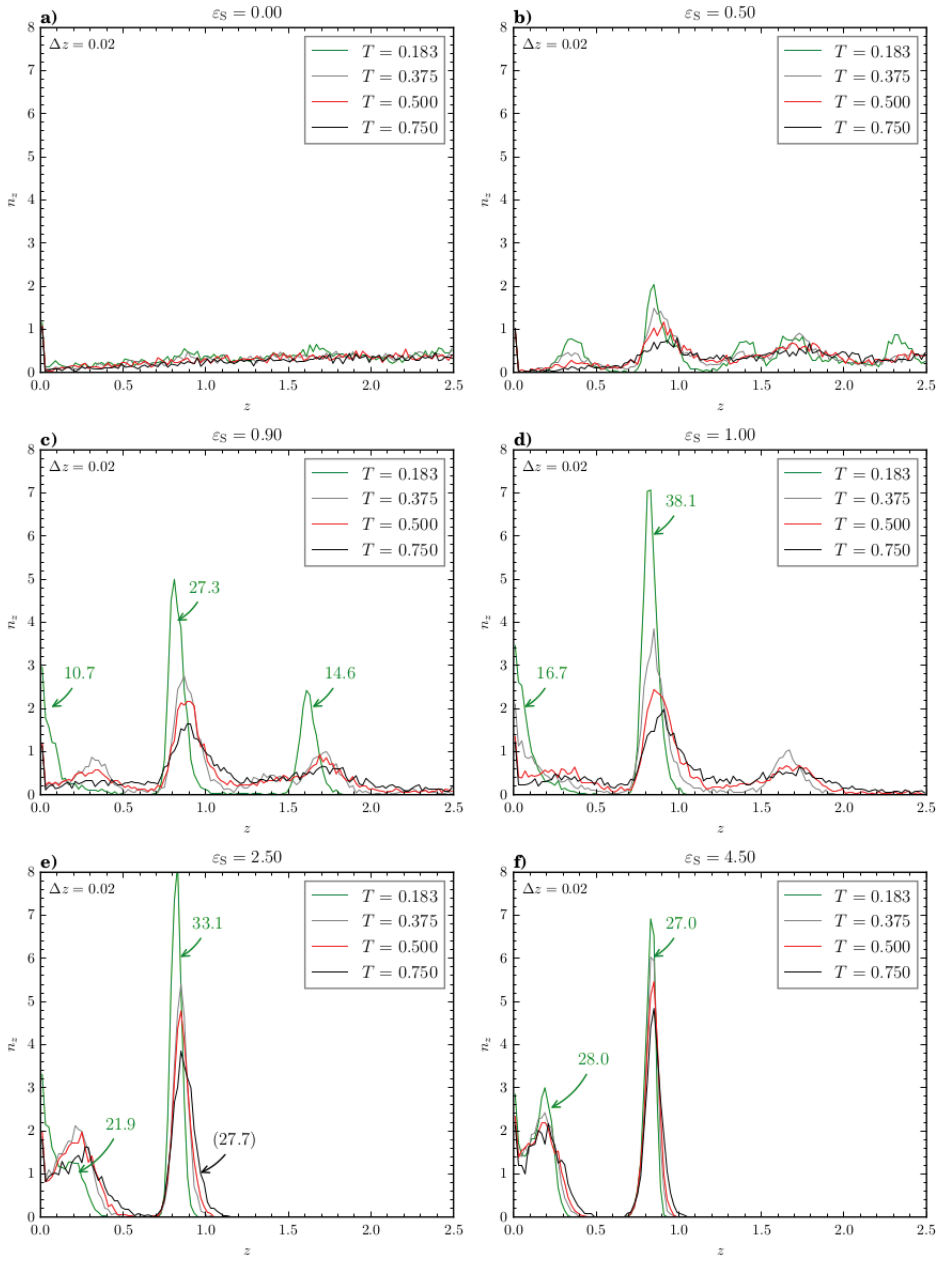

Figure 5.18: The normalized histogram n_z of the monomer height is shown for temperatures $T = \{0.18, 0.38, 0.50, 0.75\}$ at six adsorption strengths $\varepsilon_S = \{0.00, 0.50, 0.90, 1.00, 2.50, 4.50\}$. The presented data is obtained from 100 structures for each parameter pair. Numbers at peaks indicate the average number of monomers found in one layer of the HOAC3 phase c), the HOAC2 phase d),e) and in the AZ phase f).

$T = \{0.38, 0.50, 0.75\}$ at adsorption strength $\varepsilon_S = 0.90$ correspond to the polymer phases ASDPw, ASD and AGb, respectively. Although these phases are distinguished by transition signals in the specific heat they exhibit common structural behavior in terms of the height distribution: In Fig. 5.18 c) at least three distinct peaks are observed for each temperature. With increasing temperature, peaks indicating the second and third layer are shifted to slightly larger heights. For the ASDPw and ASD phase ($T = 0.38, 0.50$) an additional peak forms at about $z = 0.3$. A comparison with histograms at higher ε_S value, see Fig. 5.18 e), f), suggests that this peak at about $z = 0.3$ is caused by monomers which are lifted off from the hexagonal centers due to the formation of *zig-zag* bonds. This conjecture is supported by the representative conformation of the ASDPw shown in Fig. 5.12, monomers close to the surface of the semi-spherical conformation align to the pattern by forming *zig-zag* bridges.

Even more interesting, we found that the footprint like signature for *zig-zag* bonds is also found for low adsorption strength $\varepsilon_S = 0.50$, Fig. 5.18 b), where the monomer is in the semi-spherical droplet like patterned phases. This means that the regime of highly oriented structures with triangular layering is enclosed by phases that exhibit *zig-zag* bonds. We, therefore, conclude that in general this *zig-zag* type of pattern recognition is more stable and less parameter sensitive. If the surface interaction is turned off, no signatures are found for the AID phase, see Fig. 5.18 a), since the icosahedron is free to tilt about the grafted monomer which is located on surface of the structure. Hence, the formation of triangular overlayers in comparison to pattern recognition via *zig-zag* bond is a very specific phenomenon which distinguishes the adsorbed compact layered structures from all other phases.

5.4.2 Lateral ordering: Formation of triangular overlayers

In order to examine which effects are prevalent during the formation of triangular overlayers the lateral location of monomers in the first layer of adsorbed compact structures is

investigated. The driving force of this ordering process is the surface potential. However, monomers in the first layer, which fill the hexagonal centers, contribute via the non-bonded potential to the potential landscape which is seen by monomers in the layer above. Similar to the top view of the potential presented in Fig. 3.3 a) the combined potential landscape, created by vertices and surface monomers, is presented for $\varepsilon_{\mathrm{S}} = 0.90$ at the relevant heights $z = 0.81, 0.86, 0.90$ in Fig. 5.19. Here both monomers in the surface layer and lattice vertices were considered to create the potential landscape for the upper layer. As a result the density plots exhibit a triangular instead of a hexagonal pattern. The locations of monomers in the first layer were idealized to be at the exact center of the hexagons which can be understood as an approximation to low-temperature conformations. The locations of monomers in the surface is given as $(0, 1), (\sqrt{3}, 1), (\sqrt{3}/2, 5/2)$ and $(3\sqrt{3}/2, 5/2)$. Since the Lennard-Jones interaction of these monomers is not modified by the parameter ε_{S}, the diameters of the repulsive areas (orange) are slightly larger.

In Fig. 5.19 a), b) the potential is depicted at $z = 0.81$ above the surface. Superimposed are the locations of monomers found in the height interval $0.78 \leq z \leq 0.83$ for two temperatures. The area which is magnified in a) is marked by a square in b). We found that for $T = 0.18$ the monomer locations (blue crosses) scatter closely around the potential minima (black), whereas at $T = 0.50$ monomers are found primarily between two minima (red crosses). The overview in panel b) reveals a three-fold symmetry about the origin in the clustering of red markers, indicating that monomers in the second layer reside primarily between two lattice vertices. White colored areas, adjacent to surface layer monomers, are depopulated whereas white areas between two surface vertices are populated. This effect can be partly explained by the greater repulsion of surface layer monomers, however, a similar scattering is observed for $\varepsilon_{\mathrm{S}} = 1.0$ where non-bonded interactions coincide with the surface interaction.

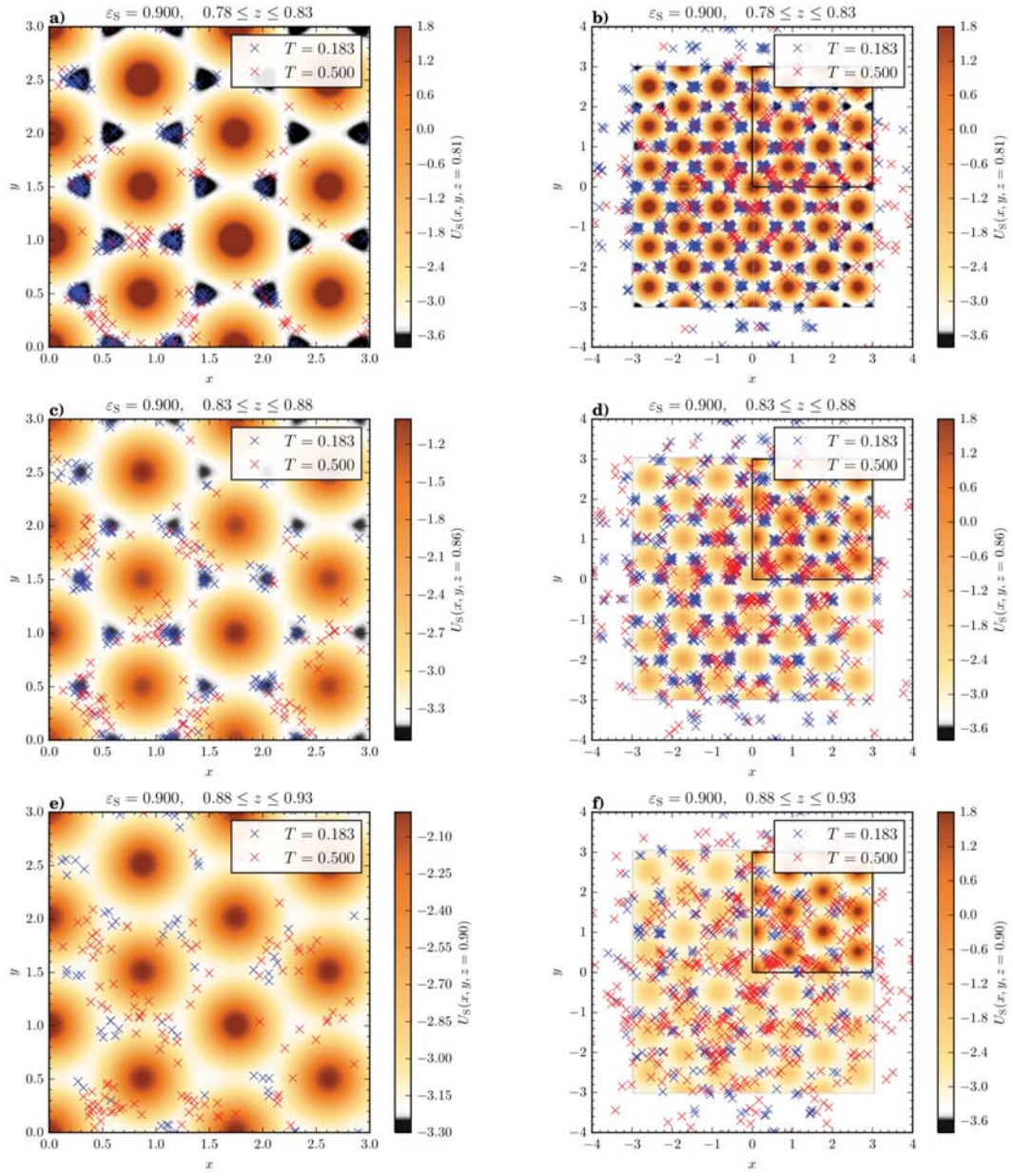

Figure 5.19: Surface parallel cuts of the potential landscape at $\varepsilon_S = 0.900$ are presented for three different heights $z = \{0.81, 0.86, 0.90\}$. The non-bonded potential of ideally positioned monomers inside the hexagonal rings contributes together with the surface potential to the potential landscape. A square in the overview graphs on the right marks the area shown in the left graph. The location of monomers in different height intervals is marked by crosses for $T = 0.18$ (blue) and $T = 0.50$ (red). The monomer coordinates were collected from 100 independent configurations for each temperature.

5.4.3 Morphology of zig-zag bonds

Outside of the specific regime for triangular overlayers at low temperatures and $\varepsilon_S \approx 0.90$, the polymer aligns to the substrate by forming zig-zag bond. In phases that are more disordered, like semispherical droplet phases, this covering type is favored because it requires less cooperativity. For smaller adsorption strength $\varepsilon_S < 0.80$ the arrangement of monomers in an triangular overlayer is entropically suppressed. If the adsorption strength is high we found that the occupation of hexagonal centers is the dominant effect.

The combined surface potential discussed in Chapter 3 favors monomers in the centers of the hexagons. Recall that if their connection is established by a *zig-zag* bonds, two competing effects arise. Bonds need either to be stretched or monomers in the hexagonal center have to lift off from the surface plane. The latter is clearly visible in the height distribution for $\varepsilon_S > 2.50$ in Fig. 5.18 e) and f). To compare this effect to bond stretching the distribution of bonds which connect monomers in the surface layer with monomers in the second layer b_{12} is presented in Fig. 5.20 a)-f) for increasing adsorption strength. Whereas squeezed bonds are found for triangular overlayers c) and d), the bond-length in the semi-spherical regime at $\varepsilon_S = 0.50$, see panel b), is slightly stretched. For the lowest temperature the distribution of the modified bond potential $U_B^{(mod)}$, see eq. (3.4), is shown as a dashed line on the second axis. Due to the flat minimum of the bond potential the distribution is peaked at zero, indicating no energetic penalty. The width of the tail of the distribution extends to about $U_B^{(mod)} < 0.50$, see Fig. 5.20 a),b) top axis . According to the equipartion theorem this energy value defines roughly a margin for the energetic penalty due to a non-optimal location in the surface potential landscape.

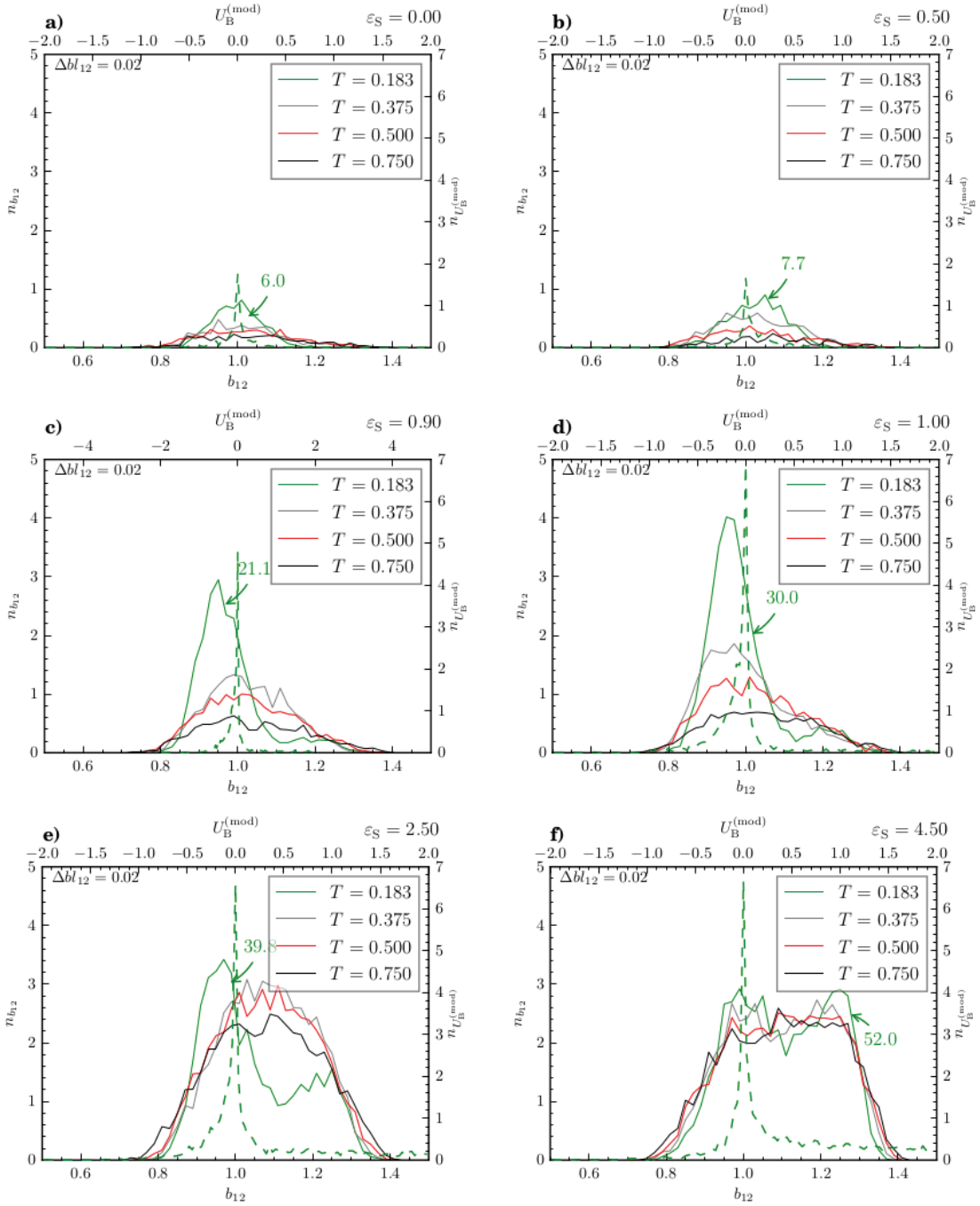

Figure 5.20: Bond-length distributions between monomers located in the surface layer and the second layer b_{12}, shown for different adsorption strengths ε_S and temperatures T. The distributions of the modified bonded potential $U_B^{(mod)}$ is shown for the lowest temperature on the second axes as a dashed line.

For high adsorption strength the bond-length distribution is much stronger pronounced towards stretched bonds $1.00 < b_{12} < 1.30$, Fig. 5.20 e), f). This can be understood in terms of larger variations of the combined surface potential. Adsorption to the surface in the HOAC2 and AZ phase provides more energy to deform bonds than in the previously discussed phases. Interestingly, the tail of the modified bond potential distribution falls off very slowly in comparison to the flank of the peak. This means that the energy in the bond is not specific. Although the *zig-zag* arrangement of three monomers is repeated over the entire homopolymer, no dominant bond-lengths are observed. Instead the linking monomer above the surface layer is shifted towards one of the hexagonal centers, leading to an asymmetry in the bridge. This notion is supported by the top view of monomers above the surface layer in Fig. 5.21. Monomers at different temperatures are shown for three different height intervals in a)-f). Monomers at heights $0.78 < z < 0.83$ are clearly scattered around the potential minima indicated with black color. At greater heights and larger temperature monomers remain located along the typical direction of a *zig-zag* bond, which coincides with the gray stripes in plot c). Occupation of the interval $0.88 \geq z \geq 0.93$ is only observed for the higher temperature. A comparison of Fig. 5.21 e) with Fig. 5.19 e) reveals that much larger ordering of monomers in the *zig-zag* configuration. Accordingly, the bond-length distribution in Fig. 5.20 f) appears to be almost temperature independent. Therefore, the geometry of this type of surface coverage is not sensitive to a change in temperature. Only a comparably small widening of the flanks in Fig. 5.20 f) indicates that energetically unfavorable squeezed or stretched bond-lengths are formed at higher temperatures.

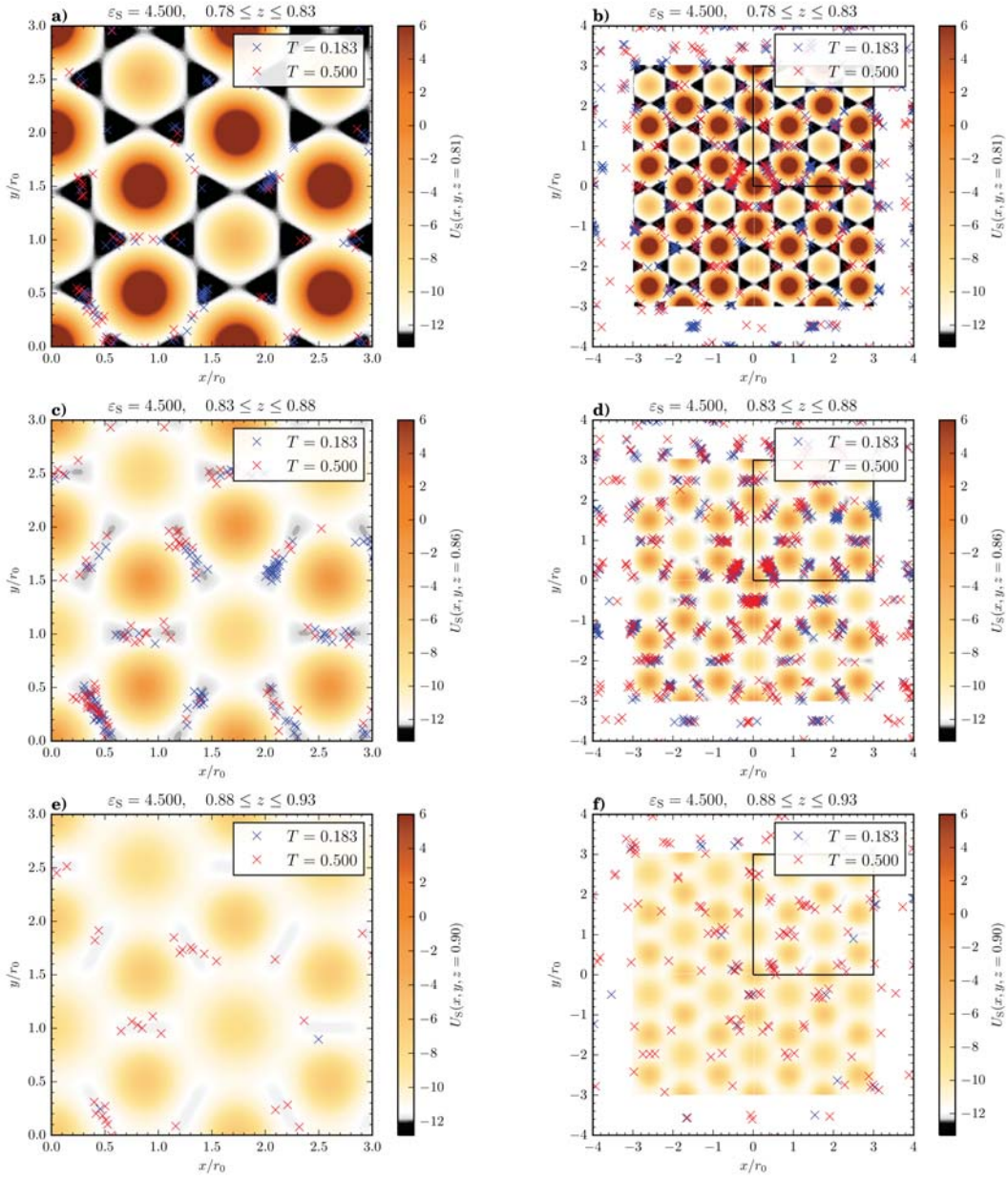

Figure 5.21: Cuts of the potential landscape together with monomer locations are presented similarly to Fig. 5.19 for $\varepsilon_S = 4.50$.

Chapter 6

Conclusion and outlook

Using Metropolis importance sampling in a parallel tempering scheme, we investigated the conformational state space of a coarse grained 13mer and a 55mer. Multiple histogram reweighting was employed to calculate an estimate for the density of states which was used to obtain thermodynamic quantities such as the specific heat. Fluctuations of structural quantities as for instance the radius of gyration, the end-to-end distance and the sphericity parameter were analyzed to identify phase transitions due to cooperative effects within the polymer chain. In order to identify adsorption effects and the recognition of the substrate pattern, different measures of surface contacts were developed.

Central to this study was to investigate how adsorption and pattern recognition depends on the relative strength of polymer-surface interaction, compared to intramolecular interactions. Therefore, a generic adsorption strength parameter was introduced in the Lennard-Jones based interaction between surface vertices and monomers. Scanning this parameter $\varepsilon_{\mathrm{S}} \in [0.0, 5.0]$ in 50 independent simulations allowed us to collect signals from different quantities in a hyperphase diagram, parametrized by temperature and adsorption strength and to construct phase transition bands.

Due to the finite character of the system these bands show finite widths which generally decrease towards lower temperatures. The analysis of fluctuations was particularly useful to locate horizontal transition bands, i.e. structural phase transitions which weakly depend on the control parameter ε_S. However, we found that for $\varepsilon_S > 0.5$ surface interactions are not negligible even for liquid- and gas-like phases. In order to obtain vertical transition lines, structural quantities were analyzed as a function of the adsorption strength. At low temperatures, derivatives with respect to T and ε_S were found to vanish. However, due to unique ground state morphologies for each structural phase, mean values of suitable order parameters converge to different characteristic values, which were used to identify locations of vertical phase-transition bands. Finally, the location of structural phases was confirmed by analyzing three dimensional visualizations of representative polymer conformations. Identifying similarities and differences between neighboring phases, refinements in the choice of order-parameters were made. On the basis of recorded coordinates for a set of representative conformations for each phase, additional information was deduced from bond length, bond angle, monomer height, and correlation of the monomer locations, leading to a characterization of phases in terms of dominant properties such as adsorbed, desorbed (A/D), expanded, globule, droplet, semispherical droplet, compact, icosahedral (E/G/D/SD/C/I), patterned, zig-zag, highly oriented (P/Z/HO), wetted and dewetted (w/d).

This work gives rise to the development of a search heuristic to classify such diverse structural information automatically which is an interesting challenge in terms of machine learning. From the comparison of results obtained for the 55mer with results for a 13mer and a continuous flat surface we found that the complexity of observed phases increases rapidly with system size and changes with the symmetry of the substrate. Such an algorithm would aid the analysis of longer or multiple grafted chains and could help to systematically investigate how different substrate patterns alter the structural behavior. More complex

order parameters such as winding numbers in semispherical droplet-like conformations may become tractable and lead to a better understanding of adsorption pathways.

Furthermore, the detailed structural information about various polymer phases is of great value for future experiments, since the generic choice of the adsorption strength parameter allows for a reparametrization and can be interpreted in multiple ways. First, it allows for the classification of different substrate materials in terms of ε_{S} using a specific polymer. Second, polymers with similar length but different side chains may be classified to predict the effect of chemical reactions on the structure formation. Third, the adsorption strength may be mapped to a change of properties in the solvent, which was treated implicitly in this study. Charges in the solution for example, may shield monomer-surface interactions, leading to an effective decrease in ε_{S}. A possible demand for such a property can be seen in the fabrication of protective coatings. In this study it was shown that highly oriented multilayer phases are observed for very specific values for the adsorption strength. Hence, precise control over this parameter may be vital in future fabrication processes.

With the structural information about all polymer phases at hand, special emphasis was put on the arrangement of solid-like phases. Starting the discussion from the limiting case of vanishing monomer-substrate interactions where icosahedral symmetries were found, flatting of droplet conformations into a dewetted and wetted semispherical shape was observed as the surface adsorption strength was increased. During this process, we saw that the interaction with the surface first broke the internal symmetry of the polymer, but induced recognition of the pattern by wetted structures at sufficiently high interaction strengths. Since at low temperatures energetic ordering effects dominate, the potential landscape created by surface vertices was analyzed. Considering the polymer approaches adsorbed phases from high temperatures, we found that monomers investigate the surface and are attracted by the centers of the hexagonal substrate. However, competing effects of bonded and non-bonded interactions lead to a challenging optimization problem. Depending on the adsorption strength,

different adsorption strategies were identified. Most remarkable is the formation of highly oriented, triangular crystal-like structures, where the onset of crystal growth into the direction perpendicular to the surface was seen. Formation of hcp and fcc lattices was found in a narrow adsorption strength regime, where $\varepsilon_S < 1.0$. In this context the influence of different side chains is not yet known. Therefore, a comparison between the coarse-grained model, considered here, and an atomistic simulation at these particular parameter values promises new insights. At higher adsorption strengths two dimensional triangular film-like structures were found. However, it was unexpected that these triangular phases are embraced by patterned phases where the formation of *zig-zag* bridges dominates. Form the analysis of the spatial coordinates at phase specific heights above the surface, it is concluded that the formation of *zig-zag* bonds requires less cooperativity, allowing for a local recognition of the pattern. This property was observed in structural phases with internal disorder such as semi-spherical droplets and globule conformations, but also as a quenching effect at high adsorption strengths, where strong barriers between local minimas of the potential are created by surface vertices.

Moreover, conflicting ordering effects of the FENE potential and the combined surface potential were discovered, which lead to subtle changes in the location of monomers, depending on the surface parameter but also on temperature. Thus, we concluded that shifts in the free-energy minimum due to entropic effects are important to the pattern recognition process. To extend the discussion of ordering effects by the surface potential to finite temperatures, measurements of the potential of mean force as a function of spatial coordinates are desirable. These measurements, however, require that entropically suppressed states close to surface vertices are sampled efficiently. In this context advanced generalized-ensemble methods are a suitable tool to overcome this challenging problem.

In order to study the stabilizing effect of patterned polymer films, we suggest repeating our simulations on flexible sheets, incorporating thermal fluctuations of the substrate. Here,

surface vertices were fixed and not affected by the finite temperature of the environment. To mimic the surface of bulk material, monomers were not allowed to penetrate the surface. Realistic simulations of polymer chains grafted on small graphene sheets would require suitable bending potentials for the substrate and a common length scale if a coarse-grained approach is used. In this case a proper coarse-graining of the substrate pattern needs to be developed.

Bibliography

[1] K.S. Novoselov, V.I. Fal'ko, L. Colombo, P.R. Gellert, M.G. Schwab, K. Kim, *Nature* **490**, 192–200 (2012)

[2] R.P. Ramasamy, H.R. Luckarift, D.M. Ivnitski, P.B. Atanassov, G.R. Johnson, *Chem. Commun.* **46**, (33) 6045-6047 (2010)

[3] M. Kim, N.S. Safron, C. Huang, M.S. Arnold, P. Gopalan, *Nano Lett.* **12**, 182–187 (2012)

[4] K. Hu, D.D. Kulkarni, I. Choi, V.V. Tsukruk, *Prog. Poly. Sci.* **39**, 1934–1972 (2014)

[5] S.W. Sides, G.S. Grest, M.J. Stevens, *Phys. Rev. E* **64**, 050802 (2001)

[6] D.B. Velusamy, R.H. Kim, S. Cha, J. Huh, R. Khazaeinezhad, S.H. Kassani, G. Song, S.M. Cho, S.H. Cho, I. Hwang, J. Lee, K. Oh, H. Choi, C. Park, *Nature Comm.* **6**, 8063 (2015)

[7] J.R. Potts, D.R. Dreyer, C.W. Bielawski, R.S. Ruoff, *Polymer* **52**, 5–25 (2011)

[8] M. Alexandre, P. Dubois, *Mater. Sci. Eng.* **28**, 1–63 (2000)

[9] T. Vogel, M. Bachmann, W. Janke, *Phys. Rev. E* **76**, 061803(1-11) (2007)

[10] T. Vogel, J. Gross, M. Bachmann, *J. Chem. Phys.* **142**, 104901(1-8) (2015)

[11] J. Gross, T. Vogel, M. Bachmann, *Phys. Chem. Chem. Phys.* **17**, 30702-30711 (2015)

[12] S. Karalus, W. Janke, M. Bachmann, *Phys. Rev. E* **84**, 031803(1-12) (2011)

[13] M. Möddel, W. Janke, M. Bachmann, *Phys. Rev. Lett.* **112**, 148303 (2014)

[14] K. Qi, B. Liewehr, T. Koci, B. Pattanasiri, M. Williams, M. Bachmann *(In preparation)*

[15] B. Liewehr, M. Bachmann *J. Phys: Conf. Ser.* **686**, 012002(1–8) (2016)

[16] B. Pattanasiri, B. Liewehr, M. Bachmann, *Phys. Proc.* **68**, 90–94 (2015)

[17] C.E. Shannon, W. Weaver, *The Mathematical Theory of Communication* (University of Illinois Press, Urbana, 1948)

[18] E.T. Jaynes, *Phys. Rev.* **106**, 620 (1957)

[19] S. Schnabel, M. Bachmann, W. Janke, *J. Chem. Phys.* **131**, 124904 (2009)

[20] S. Schnabel, T. Vogel, M. Bachmann, W. Janke, *Chem. Phys. Lett.* **476**, 201 (2009)

[21] D.T. Seaton, T. Wüst, D. P. Landau, *Comp. Phys. Comm.* **180**, 587 (2009)

[22] R. Eisenschitz, F. London, Zeitschrift für Physik **60**, (78): 491-527 (1930)

[23] F. London, *Z. Phys.* **63**, (34): 245 (1930)

[24] F. London, *T. Faraday Soc.* **33**, 826 (1937)

[25] J.E. Lennard-Jones, *Proc. Phys. Soc.* **43**, 461 (1931)

[26] T.H.K. Barron, C. Domb, *Proc. R. Soc. Lond. A* **227**, 447–465 (1955)

[27] R.B. Bird, C.F. Curtiss, R.C. Armstrong, O. Hassager, *Dynamics of Polymeric Liquids* (Wiley, New York 1987)

[28] K. Kremer, G.S. Grest, *J. Chem. Phys.* **92**, 5057–5086 (1990)

[29] A. Milchev, A. Bhattacharaya, K. Binder, *Macromolecules* **34**, 1881–1893 (2001)

[30] M.J. Williams, M. Bachmann, *Phys. Rev. Lett.* **115**, 048301(1-5) (2015)

[31] K. Qi, M. Bachmann, *J. Chem. Phys.* **141**, 074101 (2014)

[32] J.C.S. Rocha, S. Schnabel, D.P. Landau, M. Bachmann, *Phys. Rev. E* **90**, 022601 (2014)

[33] D.T. Seaton, S. Schnabel, D.P. Landau, M. Bachmann, *Phys. Rev. Lett.* **110**, 028103 (2013)

[34] J. Gross, T. Neuhaus, T. Vogel, M. Bachmann, *J. Phys. Chem.* **138**, 074905 (2013)

[35] T. Koci, M. Bachmann, *Phys. Rev. E* **92**, 042142(1-9) (2015)

[36] R.H. Swendsen, J.-S. Wang, *Phys. Rev. Lett.* **57**, 2607 (1986)

[37] C.J. Geyer, in *Computing Science and Statistics*, Proceedings of the 23rd Symposium on the Interface, p. 156. (1991)

[38] K. Hukushima, H. Takayama, K. Nemoto, *Int. J. Mod. Phys. C* **7**, 337 (1996)

[39] U.H.E. Hansmann, *Chem. Phys. Lett.* **281**, 140 (1997)

[40] A.M. Ferrenberg, R.H. Swendsen, *Phys. Rev. Lett.* **63**, 1195 (1989)

[41] S. Kumar, D. Bouzida, R.H. Swendsen, P.A. Kollman, J.M. Rosenberg, *J. Comput. Chem.* **13**, 1011 (1992)

[42] S. Schnabel, D.T. Seaton, D.P. Landau, M. Bachmann, *Phys. Rev. E* **84**, 011127(1-4) (2011)

[43] T. Li, K. Park, *Comput. Theor. Polym. S.* **11**, 133–142 (2001)

[44] M. Möddel, W. Janke, M. Bachmann *Macromolecules* **44**, 9013–9019 (2011)

[45] N. Metropolis, A.W. Rosenbluth, M.N. Rosenbluth, A.H. Teller, E. Teller, *J. Chem. Phys.*, **21**, 1087-1092 (1953)

[46] Pacheco P S, *An Introduction to Parallel Programming*, (Morgan Kaufmann, 2011)

[47] `https://www.open-mpi.org/community/lists/` (accessed, Jan. 2016)

[48] G. Marsaglia, A. Zaman, *Stat. Probabil. Lett.* **9**, 35 (1990)

[49] D. P. Landau, K. Binder, *A Guide to Monte Carlo Simulations in Statistical Physics*, 4th ed. (Cambridge, New York, 2015)

[50] M. Bachmann, *Thermodynamics and Statistical Mechanics of Macromolecular Systems* (Cambridge University Press, New York, 2014)